Particle Image Velocimetry Correlation Signal-to-noise Metrics, Particle Image Pattern Mutual Information and Measurement uncertainty Quantification

Zhenyu Xue

Thesis submitted to the faculty of the Virginia Polytechnic Institute and State University in partial fulfillment of the requirements for the degree of

Master of Science
In
Mechanical Engineering

Pavlos P. Vlachos, Chair

John J. Charonko, Co-Chair

Sunghwan Jung

John J. Socha

08-14-2014
Blacksburg, VA

Keywords: PIV, SNR, Mutual information, Uncertainty quantification

Particle Image Velocimetry Correlation Signal-to-noise Metrics, Particle Image Pattern Mutual Information and Measurement uncertainty Quantification

Zhenyu Xue

ABSTRACT

In particle image velocimetry (PIV) the measurement signal is contained in the recorded intensity of the particle image pattern superimposed on a variety of noise sources. The inherent amount of signal mutual information between consecutive images governs the strength of the resulting PIV cross correlation and ultimately the accuracy and uncertainty of the produced PIV measurements. Hence we posit that the correlation signal-to-noise-ratio (SNR) metrics calculated from the correlation plane can be used to quantify the quality of the correlation and the resulting uncertainty of an individual measurement. A new SNR metric termed "mutual information" (MI) which quantifies the amount of common information (particle pattern) between two consecutive images is also introduced and investigated. This measure provides a direct estimation of the apparent $N_I F_I F_O$ parameter of an image pair providing an alternative approach towards uncertainty estimation but also connecting the current development to one of the most fundamental principles of PIV and the previous established theory. We extend the original work by Charonko and Vlachos and present a framework for evaluating the correlation strength using a set of different metrics, which in turn are used to develop models for uncertainty estimation. Several corrections have been applied in this work. The metrics and corresponding models presented herein are expanded to be applicable to both standard and filtered correlations by applying a subtraction of the minimum correlation value to remove the effect of the background image noise. In addition, the notion of a "valid" measurement is redefined with respect to the correlation peak width in order to be consistent with uncertainty quantification principles and distinct from an "outlier" measurement. Finally the type and significance of the error distribution function is investigated. These advancements lead to robust uncertainty estimation models, which are tested against both synthetic benchmark data as

well as actual experimental measurements. In this work, $U_{68.5}$ uncertainties are estimated at the 68.5% confidence level while U_{95} uncertainties are estimated at 95% confidence level. For all cases the resulting calculated coverage factors approximate the expected theoretical confidence intervals thus demonstrating the applicability of these new models for estimation of uncertainty for individual PIV measurements.

Table of Content

List of Figures

List of Tables

1 Introduction

Particle Image Velocimetry (PIV) is a non-invasive, quantitative, flow visualization tool developed to measure fluid velocities over a wide range of length and time scales. The technique typically employs micron-size flow tracer particles, which are illuminated by a pulsed laser and imaged with a digital camera. Processing algorithms are then used to determine the displacement of the particle patterns within an image sequence and to estimate the velocity field [1]. Refinements over the past decades improved the robustness and accuracy of this technique. Currently, the term PIV is used to encompass the extensive family of methods that are based on evaluating the particle patterns displacement using statistical cross-correlation of consecutive image with high number density flow tracers[2].

However, the development of more and more sophisticated PIV methods far outpaced our ability to quantify the PIV measurement uncertainty. As a result, despite the numerous applications, theory, and contributions, there is currently no widely accepted framework for reliable quantification of PIV measurement uncertainty. The situation is exacerbated by the fact that PIV measurements involve instrument and algorithm chains with coupled uncertainty sources, rendering quantification of uncertainty far more complex than most measurement techniques. Consequently quantitative PIV results are often received with skepticism. Therefore developing a fundamental methodology for quantifying the uncertainty for PIV is an important and outstanding challenge.

2 Literature Review

PIV was first developed in the 1980s, the initial work was done by Meynart [3]. The term particle image velocimetry (PIV) was given by Adrian and appeared on the literature for the first time in the year 1984[4]. The fundamentals of PIV theory had been studied and established by Keane and Adrian in1990s [5, 6]. From the theory, the validity of a PIV measurement depends on whether the highest peak in the cross correlation plane contains the true displacement information of the particle image pattern. Incorrect measurements occur when secondary correlation peaks are higher than the peak corresponding to the true displacement. Keane and Adrian established a parameter, termed as $N_I F_I F_O$ and showed there is a relationship between this parameter and the probability of achieving a valid measurement [7]. $N_I F_I F_O$ indicates the number of correlated particle pairs per interrogation window. It is calculated as the product of the number of effective particle image pairs captured within the interrogation region (referred to as N_I), loss of correlation due to in-plane motion (F_I) and loss of correlation due to out-of-plane displacement (F_O). They also provided a guideline that in order to have a high probability for a valid measurement the value of $N_I F_I F_O$ should be above 7-10[7]. However, many of the parameters for the calculation of $N_I F_I F_O$ are not easily measurable for an individual image in an actual experiment, to date the only method to estimate $N_I F_I F_O$ is counting the number of common particle pairs in both frames, and there is still no reliable and efficient method to directly estimate the number of correlated particle pairs for individual PIV velocity measurements.

Despite the lack of method in measuring the theoretical guideline parameter $N_I F_I F_O$, PIV technique itself has been improved rapidly during the past three decades. The introduction of digital image acquisition [1] (DPIV) provided a transformative evolution of the method and triggered its widespread use and an explosive growth of applications. Refinements over the next 20 years improved the robustness and accuracy of this technique. By applying discrete window offset[8],

image and window deformation[9, 10], consistent results are able to be provided even in high displacement, shear and rotation flow conditions. Ensemble correlation[11] and single pixel correlation[12] provide more accurate result for those steady or periodic flow cases than traditional correlation method. With the help of phase correlation method, including phase-only filter [13] and robust phase correlation [14], researchers are able to get accurate velocity estimation even with some poor quality images. Other refinements, including the development of stereoscopic (3-component) planar PIV [15, 16], iterative, and adaptive methods [17-21] help further ensure the robustness and accuracy of the technique. A comprehensive history of these improvements can be traced through early reviews [22, 23] and more recent sources[2, 7, 24, 25].

However, the uncertainty of the PIV experiment has not been comprehensively studied and understood. Most of the early efforts to estimate PIV error were based on *a-priori* approach with Monte Carlo simulation. The effect of experimental parameters such as velocity gradient, particle image diameter and image intensity, on the error of PIV measurement are studied based on sets of well generated synthetic images [26, 27]. Such approaches are subject to serious limitations and criticisms due to the lack of reliability in applying the simulation results to real experiments. Reported PIV errors based on ideal simulated images are on the order of 0.1 pixels [28]. However, this is true only under certain conditions. The error can often be much more. Error of PIV measurement is always underestimated by adopting Monte Carlo simulation due to the over idealized conditions [29].

The first attempt to tackle this problem employed an “uncertainty-surface” methodology which would be constructed by mapping the effects of selected primary error sources such as shear, displacement, seeding density, and particle diameter to the true error for a given measurement [30]. This approach is roughly analogous to a more traditional instrument calibration procedure for standard experimental instruments. The generated uncertainty surface provides the means to associate the corresponding distribution of errors to any combination of inputs of the error sources

within their parameters space, as quantified directly from the actual experiment. Ultimately in order to comprehensively quantify the uncertainty, all possible combinations of displacements, shears, rotations, particle diameters, and any other parameter used must be tested which can make this method computationally expensive. Moreover, many of the relevant parameters may not be easily obtained from a real experiment.

Sciacchitano et al. proposed a method to quantify the uncertainty of PIV measurement based on particle image matching [31]. The uncertainty of measured displacement is calculated from the ensemble of disparity vectors, which are due to incomplete match between particle pairs, within the interrogation window. This method accounts for random and systematic sources of error; however peak-locking errors and truncation errors cannot be detected. In addition, the disparity can be calculated only for particles that are paired within the interrogation window, this method cannot directly account for the effects of in plane and out of plane loss of particles (though this is reflected indirectly through a scaling by the number of matched particles) and works best for particle image patterns that have been iteratively deformed to converge on each other. Finally, to calculate the instantaneous local uncertainty, researchers need to do particle image pair detection and image matching for every interrogation spot which introduces additional computation cost.

An easy and less computational expensive method to estimate the PIV measurement uncertainty is using the primary peak ratio (PPR), namely the ratio between the highest correlation peak to the second tallest peak [32]. In early PIV papers, PPR was used as a measure of the detectability of the true displacement [5, 6]. A measurement would be considered as valid if PPR were higher than a user defined threshold (often 1.2). Based on this criterion, it was established that the product of $N_I F_I F_O$ value should be approximately 5 [33]. This establishes a clear relationship between a measure of the correlation strength (PPR) and number of correlated particle image pairs. In contrast, the PPR value is easy to compute and provides a practical measure of the quality of a cross-correlation. Hain and Kahler [34] suggest that a threshold PPR value of about 2 can reliably

avoid spurious vectors, and based on this they proposed a scheme for the optimal selection of cross-correlations across a range of interframe time delays. Similarly for extending the PIV velocity dynamic range using multiple pulse separation imaging, Persoons and O'Donovan used a weighted peak ratio value as a criterion to calculate the optimum pulse separation [35]. Recently, Charonko and Vlachos proposed an uncertainty quantification method based on PPR [32]. The relationship between the distribution of velocity error magnitude and PPR value was studied and a model for calculating the uncertainty based on the PPR value of a given measurement was developed. Using this method, the uncertainty of PIV measurement can be predicted without the *a-priori* knowledge of image quality and local flow condition. Reliable uncertainty estimation results using a phase-filtered correlation (RPC) [13, 14, 36] were shown. However for standard cross-correlation (SCC) techniques (the conventional Fourier-based cross correlation with no frequency-domain filtering), the uncertainty estimation provided by this method was not as reliable. This was attributed to the insufficient treatment of noise effects inherent to the standard cross-correlation. Another problem with this method is that the authors assumed the error distribution of PIV measurement should follow a normal distribution, and only predicted the standard uncertainty. Based on this assumption the calculated expanded uncertainties should have had a confidence level close to 68.5% at the one standard deviation level ($U_{68.5}$) and 95% at the two standard deviation level for a normal distribution (U_{95}). However, this method only succeeded in predicting the U_{95} uncertainty, and the coverage factors (percent of measurements within the predicted uncertainty bounds) were much larger than the theoretical confidence level for the $U_{68.5}$ uncertainty with both phase-filtered correlation and standard cross-correlation.

It is noticed that in traditional signal process papers, the PPR is categorized as a metric for quantifying the cross-correlation signal-to-noise ratio. Beyond the PPR other metrics exist for quantifying the cross-correlation SNR. Kumar and Hassebrook defined several signal to noise ratios

of the correlation related to peak detectability including the primary peak ratio (PPR), namely peak-to-root mean square ratio (PRMSR), and peak-to-correlation energy (PCE) [37]. All three of these metrics measure the strength of correlation but the PPR is a mostly heuristic parameter while in contrast the PCE and PRMSR are grounded to signal processing theory. However, within the scope of PIV methods, neither PCE nor PRMSR have previously been considered as measures of correlation quality.

3 Objective

In this work we extend the original work by Charonko and Vlachos [32] and we seek to quantify the PIV measurement uncertainty directly from the information contained within the cross-correlation plane. The correlation plane represents the distribution of probabilities of all possible particle image pattern displacement between consecutive frames, combined with the effect of the number of particles, the mean particle diameter and effects that contribute to loss of correlation, both in-plane and out-of-plane. In other words, the correlation plane is a surrogate of the combined effects of the various sources of error that govern the accurate estimation of a particle pattern displacement. Hence, in this thesis we will seek to establish appropriate measures that quantify the cross-correlation quality by means of signal-to-noise ratio (SNR) and establish the relationship of these metrics to the individual measurement uncertainty.

In summary, we will:

1. Define metrics for quantifying the correlation signal-to-noise ratio, we have selected the following metrics:
    1) Peak ratio (PPR)
    2) Peak to root-mean-square ratio (PRMSR)
    3) Peak to correlation energy (PCE)
    4) Entropy/ information entropy (Entropy)
    5) Mutual information between consecutive images (MI)
2. Calculated all above metrics from synthetic PIV image sets
3. Study the distribution type of the PIV measurement error
4. Calculate the upper and lower limit of both $U_{68.5}$ and U_{95} uncertainty based on the distribution we found in step 3

5. Finally, we demonstrate this measure's effectiveness in synthetic and real experimental results

4 Methodology

4.1 Cross-correlation Plane

As mentioned above, our method of estimating the PIV measurement uncertainty is based on the cross-correlation signal-to-noise ratio. The knowledge of the cross-correlation plane: how the cross-correlation plane is constructed, what are the components of the plane and what are the physical meanings of all the components must be studied before the attempt can be made.

In PIV algorithm, the displacement is calculated by finding the best matching of two consecutive particle image patterns, which is determined by the means of cross correlation[2]:

$$R(s,t) = \iint \tau_1(X,Y)\tau_2(X+s,Y+t)\,dXdY \tag{1}$$

Where s and t are the displacements in X and Y direction, $\tau_1(X,Y)$ and $\tau_2(X,Y)$ are the recorded particle image patterns, which are determined by the light intensity distribution $I_1(X,Y)$ and $I_2(X,Y)$ appear within the interrogation domains $W_1(X,Y)$ and $W_2(X,Y)$:

$$\tau_{1,2} = W_{1,2}(X,Y)\,I_{1,2}(X,Y) \tag{2}$$

Usually, the intensity field can be separated into image background noise part and particle image part, they can also be considered as the mean ($\langle I_{1,2} \rangle$) and fluctuation ($\Delta I_{1,2}$) part:

$$I_{1,2}(X,Y) = \langle I_{1,2} \rangle + \Delta I_{1,2}(X,Y) \tag{3}$$

Substitute equation 2 and 3 into equation 1, then the cross correlation can be divided into three different parts: the correlation of the mean background intensity, R_C; background noise in one frame correlated with the particle image in the other window, R_F; and the cross-correlation of the fluctuating image (particle image) intensity in both windows, R_D,. They can be expressed as:

$$R(s,t) = R_C(s,t) + R_F(s,t) + R_D(s,t) \tag{4}$$

$$R_C(s,t) = \iint W_1(X,Y) W_2(X+s,Y+t) \langle I_1 \rangle \langle I_2 \rangle dXdY \tag{5}$$

$$R_F(s,t) = \iint W_1(X,Y) W_2(X+s,Y+t) \left[\langle I_1 \rangle \Delta I_2(X+s,Y+t) + \langle I_2 \rangle \Delta I_1(X,Y) \right] dXdY \tag{6}$$

$$R_D(s,t) = \iint W_1(X,Y) W_2(X+s,Y+t) \Delta I_1(X,Y) \Delta I_2(X+s,Y+t) dXdY \tag{7}$$

The R_C part and the R_F part can be combined together, termed as R_N, which can be considered as the effect of the image background noise on the cross-correlation plane.

The cross-correlation of the fluctuating image intensity, R_D, can be further separated into two parts: ensemble mean which indicates the measured displacement $\langle R_D(s,t) | \vec{u} \rangle$ and random correlation peaks, as shown in Figure 1.

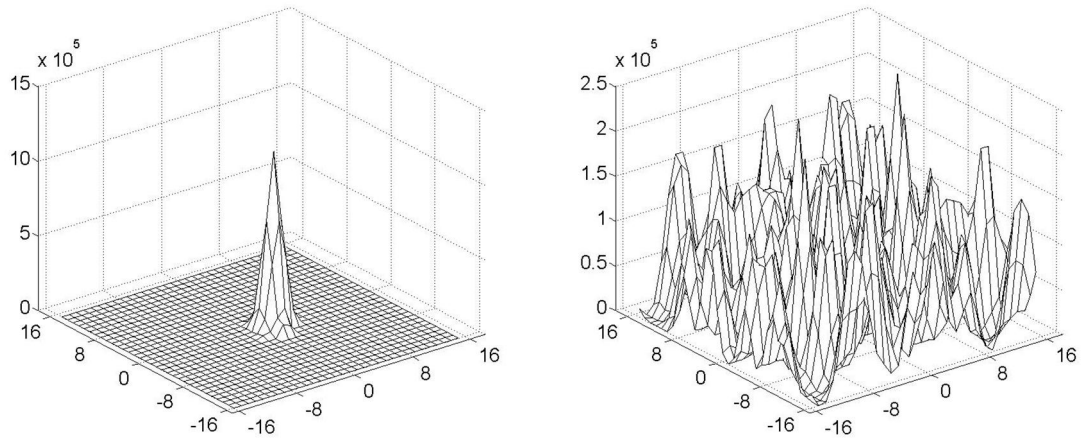

(a) (b)

Figure 1 Separation of R_D into its ensemble mean (a) and random correlation peaks (b)

4.1.1 Ensemble mean of R_D, $\langle R_D(s,t) | \vec{u} \rangle$

Usually, this part appears as a sharp peak in the cross correlation plane. The true particle pattern displacement information is contained within this peak. With a given flow field $\vec{u}$, we can write the conditional ensemble average of R_D as:

$$\langle R_D(s,t) | \vec{u} \rangle = \iint W_1(X,Y) W(X+s,Y+t) \langle \Delta I_1(X,Y) \Delta I_2(X+s,Y+t) | \vec{u} \rangle dXdY \tag{8}$$

From Particle Image Velocimetry text book[2], the ensemble cross-correlation can be expressed as:

$$\left\langle \Delta I_1(X,Y)\Delta I_2(X+s,Y+t)\,|\,\vec{u}\right\rangle = \boldsymbol{J}_{01}\boldsymbol{J}_{02}\frac{C\Delta z_{12}^{*}}{M_0^2}\tau_{00}^2 F_O(\Delta z)F_\tau(s-s_D,t-t_D) \tag{9}$$

Where $\boldsymbol{J}_{01,2}$ is the maximum value of illuminating beam intensity of frame 1 and 2 respectively, C is the tracer number density, $\Delta z_{12}^{"}$ is the thickness of the light sheet, M_0 is the nominal image magnification, τ_{00} is the total particle image intensity per unit illumination, $F_O(\Delta z)$ is the out-of-plane loss of correlation, $F_\tau(s-s_D,t-t_D)$ is the particle image self-correlation and s_D and t_D are the particle image displacement in the horizontal and vertical direction respectively. Also from the definitions given by the textbook, we know that:

$$N_I = C\Delta z_{12}^{*}\, D_I^2 \Big/ M_0^2 \tag{10}$$

$$F_I(\mathrm{s,t}) = \iint W_1(X,Y)W(X+s,Y+t)\,dXdY \Big/ D_I^2 \tag{11}$$

Where N_I is the image density, D_I is the linear dimension of interrogation area, $F_I(s,t)$ is the in-plane loss of correlation.

Substitute equation 9, 10, 11 into equation 8 we can get the final expression of the ensemble mean of R_D:

$$\left\langle R_D(s,t)\,|\,\vec{u}\right\rangle = \boldsymbol{J}_{01}\boldsymbol{J}_{02}N_I F_I(\mathrm{s,t})F_O(\Delta z)\tau_{00}^2 F_\tau(s-s_D,t-t_D) \tag{12}$$

Thus from this theoretical derivation, it is clear that the height of the ensemble mean of the cross-correlation of the fluctuating image intensity, $\left\langle R_D(s,t)\,|\,\vec{u}\right\rangle$ is proportional to the production of the laser beam intensity $\boldsymbol{J}_{01,2}$, image density N_I, in-plane loss of correlation $F_I(\mathrm{s,t})$, and out-of-plane loss of correlation $F_O(\Delta z)$.

4.1.2 Shape of Ensemble mean of R_D, $\left\langle R_D(s,t)\,|\,\vec{u}\right\rangle$

The remaining part $\tau_{00}^2 F_\tau(s-s_D,t-t_D)$ in equation 12 is the particle image self-correlation. The shape of the peak corresponding to the true displacement is determined by the convolution of this

part with the local velocity gradient. For calculation convenient, researchers usually use circle to approximate the shape of the peak, and the width (diameter) can be calculated by[2]:

$$d_D = \sqrt{2d_\tau^2 + f(a)} \tag{13}$$

Where d_τ is the particle image diameter and *f(a)* is function of the local velocity gradient *a*, where the function *f* is determined by the type of flow.

4.1.3 Random correlation peaks $R_D(s) - \langle R_D(s) | \mathrm{u} \rangle$

The random correlation peaks represent correlations between distinct randomly matched particle pairs, which can be considered as the noise part of the correlation. A valid measurement is obtained when the peak corresponding to the true displacement is higher than the highest random noise peak. If we take the signal part of the cross correlation plane as the primary peak height, the expected signal-to-noise ratio (SNR) should be relatively high to insure a successful measurement.

Following the work by Kumar and Hassebrook three measures are introduced to quantify the correlation SNR. They are the primary peak ratio (PPR), the peak to root mean square ratio (PRMSR) and the peak to correlation energy (PCE).

The primary peak ratio (PPR) is defined as the ratio between the height of the primary peak and the height of the second tallest peak, it is calculated as:

$$\mathrm{PPR} = \frac{C_{\max}}{C_2} \tag{14}$$

The signal part is C_{max}, the primary peak height, and the noise part is C_2, the height of the secondary peak.

The peak to root mean square ratio (PRMSR) is defined as the ratio between the magnitude of cross correlation plane and square of the correlation plane root mean square value. The expression for PRMSR calculation is:

$$\mathrm{PRMSR} = \frac{|C_{\max}|^2}{C_{rms}{}^2} \tag{15}$$

The signal part is the magnitude of the cross correlation plane $|C_{\max}|^2$, which is calculated as the square of the primary peak height; the noise part $C_{rms}{}^2$, and is calculated as:

$$C_{rms}{}^2 = \left[\sqrt{\frac{1}{N_\Omega} \sum_{i \in \Omega} |C(\mathrm{i})|^2} \right]^2 \tag{16}$$

Where Ω indicates the group of points on the correlation plane where the correlation value of those points are lower than half of primary peak height.

The peak to correlation energy (PCE) is defined as the ratio between the magnitude of cross correlation plane and the correlation energy, which can be calculated as:

$$\mathrm{PCE} = \frac{|C_{\max}|^2}{E_c} \tag{17}$$

The magnitude of the correlation plane $|C_{\max}|^2$ is the signal part; the noise part, or correlation energy is defined as:

$$E_c = \int_{-\infty}^{\infty} |C(x)|^2 dx \tag{18}$$

However, in practice, the correlation plane has finite size. So we calculate the correlation energy as:

$$E_c = \frac{1}{W} \left(\sum_{W} |C(x)|^2 \right) \tag{19}$$

Where W is the size of the correlation plane.

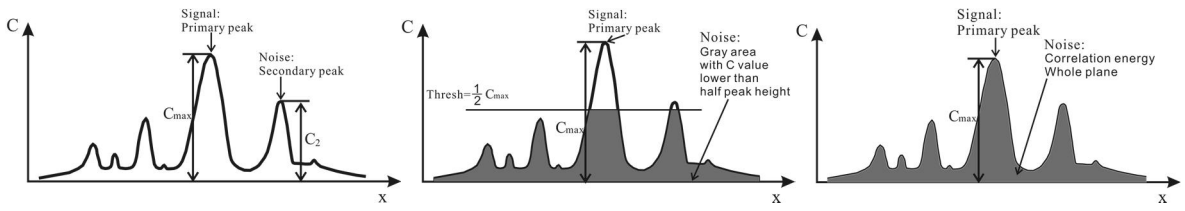

(a) (b) (c)

Figure 2 1D Graphical representation of correlation SNR: (a) PPR; (b) PRMSR; (C) PCE.

Figure 2 shows one-dimensional graphical representation of all three SNR metrics. Effectively these metrics measure the detectability of the primary peak with respect to alternative correlations.

However, in contrast to the PPR which is an *ad-hoc* metric, the PRMSR and PCE are amenable to analytical derivation if the signal statistical properties are known [37], hence they offer the potential for developing a corresponding theoretical foundation for the uncertainty estimation. This aspect however will not be pursued during this work.

Another signal to noise ratio measure considered herein is the cross-correlation entropy or information entropy [38]. This is based on the notion that if perfect matching between two image patterns exists in the absence of any noise, the correlation will yield a single sharp peak and the correlation entropy value will be minimum. As more random correlations exist the entropy would increase. To calculate the entropy of the cross correlation plane, we first construct the histogram of the correlation plane based on the correlation value of every point on the plane. In our work, we use 30 bins to build the histogram. After the histogram is generated, the probability of finding one point within a certain bin is calculated as:

$$p_i = \frac{\#\text{ of points @ bin } i}{\text{Total \# points of whole plane}}$$

Then the entropy of the cross correlation plane was calculated as:

$$\text{Entropy} = \sum_{i=1}^{30} p_i \log \frac{1}{p_i} = -\sum_{i=1}^{30} p_i \log p_i \tag{20}$$

4.2 Role of image background noise on correlation SNR

As mentioned in previous sections, the information about the true displacement in the correlation plane is contained in the correlation of the fluctuating intensities, and the random correlation peaks are also come from the correlation of the fluctuating intensities only. The image background noise has no contribution to neither the signal part nor the noise part of the cross correlation. So in order to obtain a more accurate signal-to-noise ratio of the cross-correlation plane, eliminating the effect of image background noise is necessary.

It is common practice to subtract the image mean intensity before performing a cross-correlation, which would effectively remove all contributions from the background and only provide R_D. However in practice this does not always hold true due to various illumination artifacts and imaging distortions. Although for the estimation of the true displacement such residuals would have negligible effect, in contrast for the calculation of the correlation SNR they can profoundly affect the metrics. The reason for this can be simply illustrated by the fact that if any two arbitrary measures are increased by the same constant offset, although their difference remains the same, their ratio is decreasing. By definition the SNR is a ratio of the measure of the signal to the noise levels hence would be subject to the same effect. As a result, in their work Charonko and Vlachos [32] showed that the standard correlation suffered from this effect and performed inferiorly to the phase filter correlation which in turn is largely immune to such effects. Hence in order to address this limitation and provide more robust estimation of the different correlation metrics we propose to subtract the minimum value of the correlation plane.

Figure 3 demonstrates this using an example of a particle image with and without background noise. The corresponding cross correlation planes of these two images sets are shown in Figure 4 a and b. The minimum correlation value of the cross correlation is on the order of 10^6. After we subtract the correlation plane of Figure 4b (R_D) from Figure 4a (R), the left plane Figure 4c can be considered as the correlation related to background image noise, the R_C and R_F term together. The mean value of this plane is also close to 10^6. Subtraction of the minimum correlation value from the correlation plane effectively eliminated the effect of background image noise on the cross correlation plane without having to explicitly filter the image regions.

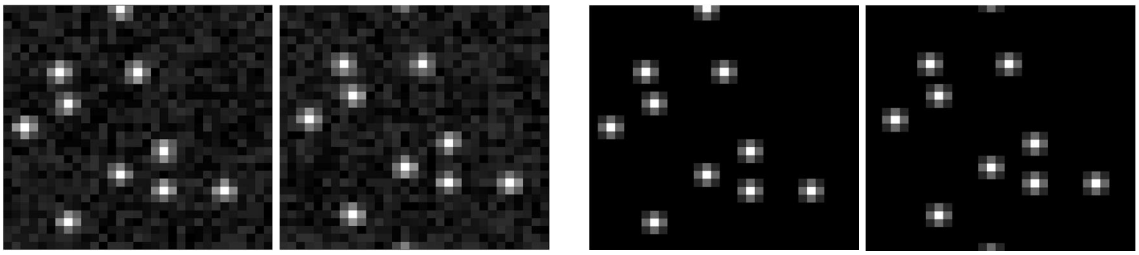

(a) (b)

Figure 3 Particle image sets examples (a) with background noise; (b) same particle images without background noise

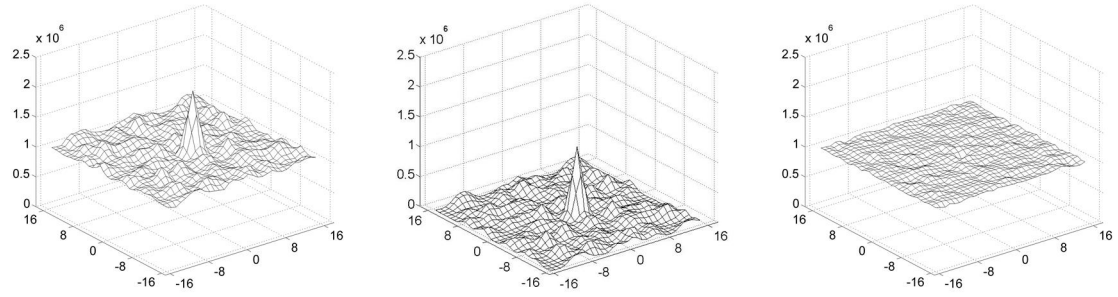

(a) (b) (c)

Figure 4 (a) cross correlation plane of particle images with background noise (b) cross correlation plane of particle images without background noise (c) the correlation plane related to background noise

4.3 Mutual Information (MI) and relationship to $N_I F_I F_O$

In the textbook, the $N_I F_I F_O$ appears when considering conditional averages of the correlation, and the guideline is based on results from Monte Carlo simulations[2]. However, for a real experiment, it is still useful to know the number of correlated particle pairs for each measured vector, not just on average, so that an estimate can be made of whether the cross correlation is strong enough to provide a successful measurement. Therefore, our work is essentially an extension of $N_I F_I F_O$ to instantaneous correlations. However, many of the parameters are not easily measurable for an individual image in an actual experiment, for example, the tracer particle number density C

might be different from one interrogation region to another and the out-of-plane displacement Δz cannot be measured using a single planar 2D PIV measurement, thus making $N_I F_I F_O$ difficult to estimate in real data.

As discussed earlier, the correlation peak height (height of the ensemble mean of R_D, $\langle R_D(s,t)|\vec{u}\rangle$) is proportional to the product of the image density N_I, the out-of-plane loss of correlation F_O and the in-plane loss of correlation F_I, and the shape of the peak is determined by the particle image self-correlation and displacement distribution. Based on this insight we introduce a new measure of the correlation SNR which we term Mutual Information (MI). MI is defined based on a ratio of contributions to the correlation peak as:

$$\frac{\text{Contribution of all correlated particle pairs}}{\text{Contribution of one correlated particle pair}} = \text{Total number of correlated particle paris} = \text{Mutual information}$$

MI provides the means to directly calculate the apparent $N_I F_I F_O$ from the information contained within the correlation plane. The calculation of MI entails dividing the magnitude of highest peak in the cross correlation by the height of the autocorrelation of the "mean" particle with a diameter determined from the image autocorrelation[39]. A schematic of the calculation flow chart is shown below (Figure 5). This standard Gaussian particle is not a real particle selected from the ROI subregions, but is instead an equivalent synthetic particle constructed based on the mean particle properties of each correlate subregion. The steps of building this "equivalent synthetic particle" will be explained in detail in the following section. Notice that we can calculate MI value from either the whole correlation plane or only the magnitude part of the correlation plane, and the difference between these two methods is negligible, as shown in Figure 5. The MI values of measurements processed by SCC are calculated using the whole correlation plane, and the MI values of measurements processed by RPC are calculated by using only the magnitude part. The detailed calculation steps will be discussed in the following paragraphs in this section.

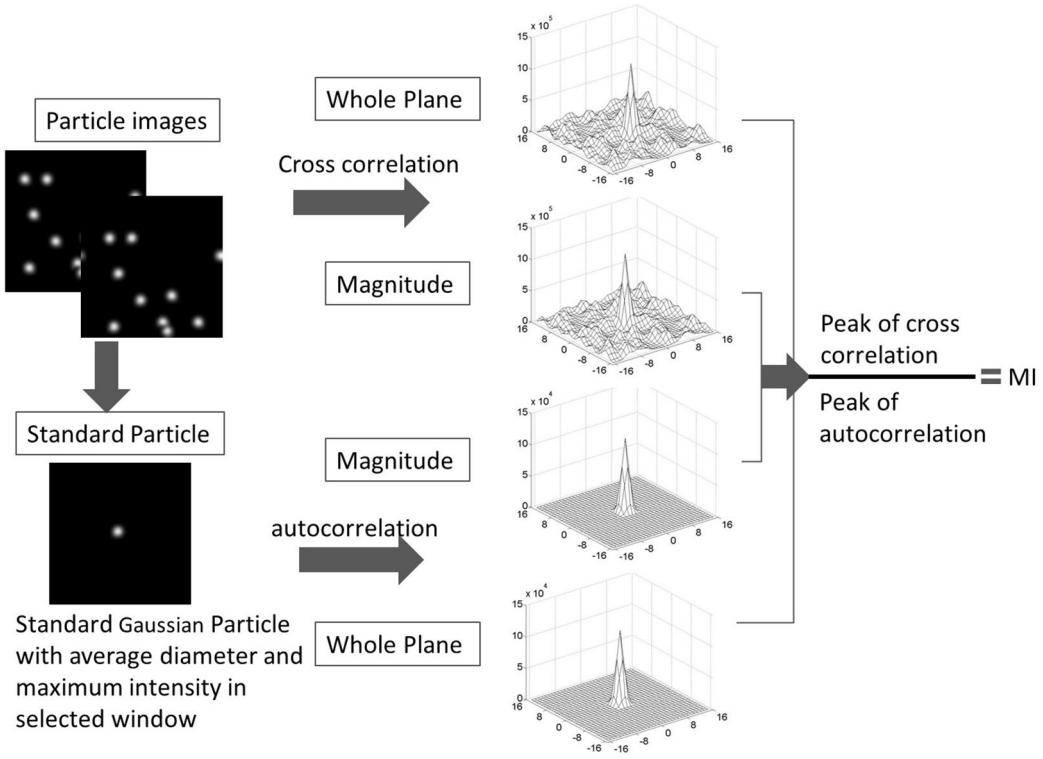

Figure 5 Schematic illustrating the calculation of MI. MI equals to 10 in this example using ten particles located an integer positions and shifted by an integer displacement with no loss of correlation.

The image of the equivalent synthetic Gaussian particle can be written as:

$$P(X,Y)=\iint J_0 e^{\left(-8\left(\frac{(X-X')^2}{d_0^2}+\frac{(Y-Y')^2}{d_0^2}\right)\right)}\otimes\delta\left(X'-x_p,Y'-y_p\right)dX'dY' \tag{21}$$

where J_0 and d_0 are the intensity and diameter, and x_p and y_p are the particle center coordinates. In practice, J_0 is the average value of the maximum intensity of all particles in each of the two correlated interrogation regions. We apply a three point Gaussian fit on the autocorrelation of the particle images in the interrogation domain to get the "mean" particle diameter of each correlation subregion, and d_0 is the average of the "mean" diameters found for each of the two correlated interrogation regions[40]. Then we substitute J_0 and d_0 into equation (21) to build the equivalent synthetic particle. The autocorrelation of this particle is then calculated as:

$$A(s,t)=\iint P(X,\mathrm{Y})\times P(X+s,Y+t)\,dXdY \tag{22}$$

The height of the autocorrelation peak A_0 is the magnitude of the peak, which should reflect the contribution of one correlated particle pair to the final height of the cross correlation primary peak. It can be calculated as:

$$A_0=\frac{1}{16}J_0{}^2 d_0{}^2\pi \tag{23}$$

We can also substitute J_0 and d_0 into this equation to calculate the contribution from one correlated particle pair. However, this equation comes from the autocorrelation of a continuous 2D Gaussian function, while the particle images in digital PIV are discrete. As a result, the autocorrelation peak height calculated by directly using equation (23) will be slightly different from the result calculated by the FFT based correlation. Although the computational cost of using the FFT based correlation is higher than directly using the analytical form, to keep our algorithm consistent, we keep using the FFT based correlation to estimate the contribution of one correlated particle pair in this work.

We can write the analytical form of the cross correlation plane for image 1 and image 2 as:

$$R(s,t)=\iint I_1(X,Y)I_2(X+s,Y+t)\,dXdY \tag{24}$$

where I_1 and I_2 are the intensity distributions of the two interrogation regions, and *s* and *t* are the displacements in *X* and *Y* directions respectively. After removing the background image noise effect (details of this will be provided in a later section) we can consider the image as the summation of all particles within the window area:

$$I_1=\iint\sum_{p_1}J_{i1}e^{\left(-8\left(\frac{(X-X')^2}{d_{i1}{}^2}+\frac{(Y-Y')^2}{d_{i1}{}^2}\right)\right)}\otimes\delta\left(X'-x_{p_i},Y'-y_{p_i}\right)dX'dY' \tag{25}$$

$$I_2=\iint\sum_{p_2}J_{i2}e^{\left(-8\left(\frac{(X-X')^2}{d_{i2}{}^2}+\frac{(Y-Y')^2}{d_{i2}{}^2}\right)\right)}\otimes\delta\left(X'-\left(x_{p_i}+\Delta x_i\right),Y'-\left(y_{p_i}+\Delta y_i\right)\right)dX'dY' \tag{26}$$

where p_1 and p_2 are the numbers of particles in image 1 and 2, J_i and d_i are the intensity and diameter of the i^{th} particle, x_{p_i} and y_{p_i} are the location the i^{th} particle in the first image, and Δx_i and

Δy_i are the displacement components of the i^{th} particle (note that the displacement of every particle within the interrogation regions might be different due to shear or rotations). As a result, we can write the expression for the number of correlated particle pairs, p_c as:

$$p_c = N_I F_I(s,t) F_O(\Delta z) F_\Delta(s,t) \tag{27}$$

$F_\Delta(s,t)$ is the loss of correlation due to local gradients over a finite measurement area, which can be calculated as:

$$F_\Delta(s,t) = \frac{1}{A_I} \int_{A_I} \delta\left(s - \Delta x(x,y), t - \Delta y(x,y)\right) dxdy \tag{28}$$

where A_I is the area of interrogation domain, $\delta(s,t)$ is a Dirac δ-function, $\Delta x(x,y)$ and $\Delta y(x,y)$ are the displacement components by the velocity field $\vec{u}$ of a particle originally located at (x,y) in the first frame to a position $x' = x + \Delta x$ and $y' = y + \Delta y$ in the next frame. So for any non-uniform flow field, such as simple shear flow, the $F_\Delta(s,t)$ will be less than 1, which means the value of p_c will decrease due to the loss of correlation because of the local velocity gradients. However, for brevity we will continue to refer to $N_I F_I F_O$ with the inclusion of the shear term being implied.

By assuming that the pulse-to-pulse variation of the laser is negligible and the correlated particles in frame 1 and frame 2 are identical ($J_{i1} = J_{i2}$ and $d_{i1} = d_{i2}$), we can show that the primary peak height of the cross correlation plane can be expressed as:

$$\begin{aligned} C_{\max} &= mag\left(\sum_{p_c} \iint J_i^2 e^{-8\left[\frac{(X - x_{p,i})^2}{d_i^2} + \frac{(Y - y_{p,i})^2}{d_i^2}\right]} \times e^{-8\left[\frac{(X - x_{p,i})^2}{d_i^2} + \frac{(Y - y_{p,i})^2}{d_i^2}\right]} dXdY \right) \\ &= \sum_{p_c} \frac{1}{16} J_i^2 d_i^2 \pi \end{aligned} \tag{29}$$

where p_c is number of correlated particles in both frames, J_i and d_i are the intensity and diameter of the i^{th} particle. Comparing (29) with(23), it is obvious that the value of $C_{\max}$ is the summation of the autocorrelation magnitude of all the correlated particle pairs within the interrogation region. Thus the number of correlated particle pairs (or the amount of mutual information) between

consecutive frames (MI) can be estimated by dividing the height of the cross correlation peak by the magnitude of autocorrelation of one equivalent synthetic particle pair, as:

$$\mathrm{MI} = \frac{C_{\max}}{A_0} = \frac{\sum_{p_c} \frac{1}{16} J_i^2 d_i^2 \pi}{\frac{1}{16} J_0^2 d_0^2 \pi} = \sum_{p_c} \frac{J_i^2 d_i^2}{J_0^2 d_0^2} \tag{30}$$

It is clear then that in the case when every correlated particle has the same intensity and diameter as the reference particle ($J_i = J_0$ and $d_i = d_0$), the MI value will be equal to p_c ($N_I F_I F_O$, also including the F_Δ term). For interrogation regions where the particle size and brightness varies, the contribution of each particle will be proportionally weighted in terms of its effect on the final correlation signal. Thus we can conclude that the MI metric does not only contain all the information of $N_I F_I F_O$, but also takes the particle size and diameter effects into account.

From the definition of the cross correlation, it is clear that during PIV processing, we correlate the intensity distribution pattern rather than every individual particle. As a result, tiny dim particles will contribute less than large bright particles to the correlation plane. However, the traditional definition of $N_I F_I F_O$ suggests that the contributions of all correlated particles are equal, regardless of the size or brightness of the particles. As long as the particle pairs match, the contribution to the correlation peak will be counted as one. Unfortunately, this is true only for ideal cases when all particles have the same intensity distribution and size. As a result, the traditional definition of $N_I F_I F_O$ does not match the actual behavior of the standard cross-correlation in a real experiment. In practice we should consider the effect of particle intensity and diameter in order to model the actual contribution of each particle toward the final correlation. As shown in equation (30), particle diameter and intensity distribution are considered in our MI calculation, suggesting that MI should more reliably characterize the quality of the particle cross-correlation for experimental data. Therefore, in the following sections, when showing the relationship between MI and $N_I F_I F_O$ using synthetic data, instead of using the $N_I F_I F_O$ value calculated based on the original definition, we use

the values scaled by the particle diameter and intensity distribution, based on equation (30). For example, if the maximum intensity of the particles in a certain region is 100, and we detect one correlated particle pair with intensity of 50, the contribution of that correlated particle will be counted as 0.25 ($(50/100)^2$) of the maximum particle when we calculate $N_I F_I F_O$.

For those vectors measured using standard cross correlation, we can directly use the cross correlation plane to calculate the mutual information. However, for phase correlation methods, the magnitude part of the correlation plane containing all the information regarding the particle diameter and brightness has been removed. As a result, MI cannot be estimated directly from the RPC correlation plane. However, this can be easily remedied. In order to calculate the mutual information of the measurements using the RPC method, instead of using the height of the primary peak on the final RPC correlation plane, for C_{max} we use the primary peak height of the original magnitude of the cross correlation before the normalization and filtering (as shown in equation (29)) which yields the same result without any loss of information.

4.4 Correlation width and definition of a valid measurements

As mentioned in previous section, the primary peak diameter can be calculated by[2]:

$$d_D = \sqrt{2d_\tau^2 + f(a)} \tag{31}$$

However, for a real PIV experiment, the average particle diameter d_τ and the effect of local velocity gradient parameter $f(a)$ are not easy to estimate. So for a given correlation plane, the correlation peak width is usually calculated by performing a three-point Gaussian fit and then computing the diameter as 4 times the standard deviation for the Gaussian distribution [41]. Using an elliptical Gaussian fit would provide a better estimation of the size for the cases when the correlation does not yield a symmetric Gaussian distribution. The location of the maximum value of that Gaussian function provides the sub-pixel displacement estimation for the PIV measurement. This is subject to the assumption that the true displacement is within the primary peak region. Thus, if the difference

between the measured displacement and true displacement (i.e. the error) is less than half of the peak diameter, the measurement should be considered as valid because the peak corresponds to the true displacement. However, previous works often use a fixed threshold value for detecting failed measurements or outliers. Outliers were identified either using a local neighbourhood statistical criterion[42] or if the difference between the measurement and the true value is larger than a pre-determined threshold, for example 0.5 or 1 pixel, regardless if the correlation peak contains the true displacement information or not. By using either approach, the conventional definition of outliers is inconsistent with the notion of error and uncertainty. For example, a wide peak at a location corresponding to the true displacement, although it could yield errors in excess of 1 pixel, would still be accurate but it would not be precise. This is because the identified displacement peak successfully matched the true measurement, but was too wide to yield a precise evaluation of the displacement. Instead, here we suggest that the criterion for a valid measurement should be based on the diameter of the correlation peak. If the error is less than half of the peak diameter, we conclude that the measurement successfully found the correct peak and it is indeed a valid measurement. Only those measurements providing the wrong primary peak are considered as invalid. An example of this "half peak diameter" criterion is shown in Figure 6.

Note that the concepts of valid measurements versus outliers are different and distinct. An outlier is determined by statistical comparison with its neighbourhood while a valid or invalid measurement should be based on an independent assessment of the measurement's success or failure, regardless of the statistical properties of the neighbourhood in which it is located. Using this model, a peak with diameter larger than a single pixel, due to particle size and large shear gradient, may be identifying the velocity distribution within the interrogation region correctly; this holds even if the highest point within the peak is located more than one pixel away from the location related to the true velocity. Thus, it should not be counted as a failure, but should instead be included as a valid measurement but with a larger uncertainty.

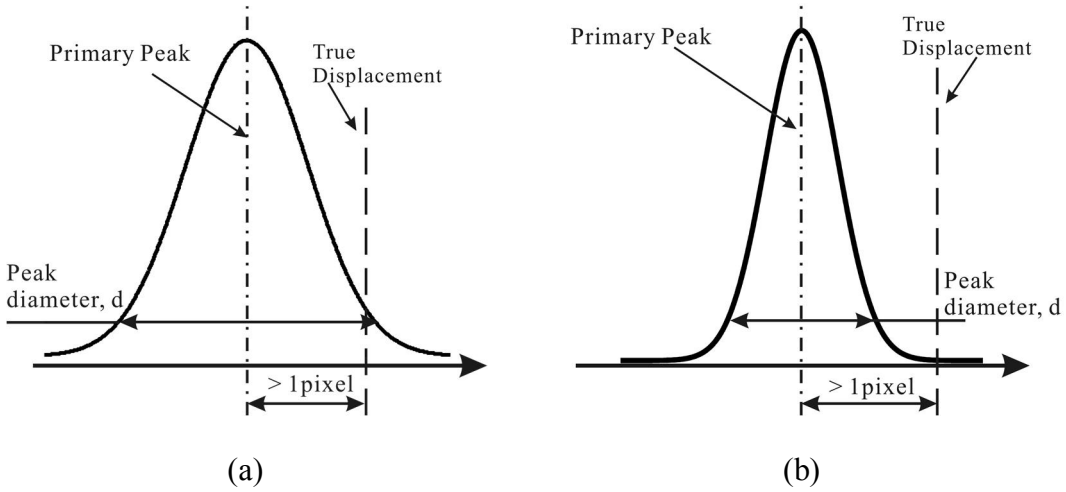

Figure 6 1-D example of half peak diameter criterion (a) good measurement; (b) outlier

4.5 Synthetic image sets

Synthetic image sets with known displacements information were used to develop the relations between the uncertainty or error distribution and MI. A separate synthetic image set with particle location information was also tested to show the relationship between calculated MI and true $N_I F_I F_O$. These particular sets were chosen as opposed to generating new images because they have previously been well characterized in the literature and are publically available, allowing for convenient comparison to past and future methods.

4.5.1 PIV standard image sets

PIV standard image sets (3D shear jet flow), were tested to show the relationship between MI and $N_I F_I F_O$. In particular, this case was selected because every particle that appears in the image has a unique ID and its position in every frame is provided. With this particle list, we are able to count the exact number of correlated particle pairs in consecutive frames, which is necessary for a comparison between the two metrics. The details can be found in the work of Okamoto *et al.* [43].

4.5.2 Turbulent boundary layer

The first data set is 100 image pairs of turbulent boundary layer flow field (Case B of the Second International PIV challenge in 2003 [44]). The image quality is: 70 particle pairs per 32X32 region with 2.6 pixel average particle diameter at the 4 standard deviations.

4.5.3 Laminar separation bubble

The second data set is 18 image pairs of laminar separation bubble flow field (Case B of the Third International PIV challenge in 2005 [45]). 25 particles per 32x32 window is the average seeding density of this data set. The average particle diameter is about 2.0 pixels. Because the providers only reported six timesteps (frames 10, 30, 50, 70, 90 and 110) of exact solution of the flow field, we correlated the particle images of symmetrically distributed frames about the given timestep when processing this data set. For example, to estimate the flow field of frame 10, we correlated frame 9 and 11 when the chosen correlation step is 2. The correlation steps we used here were 2, 4 and 6. This procedure led to some regions of the flow having very large displacements. Due to the principles of the Fourier based cross correlation, the vectors with displacements larger than half of the interrogation window size will be wrapped around and the estimated displacements will appear in the opposite direction. Although those vectors will be identified as invalid measurements based on our "half peak diameter" rule, correct peaks with the true displacement information can still be detected. To avoid this inconsistency those vectors were not included in our analysis.

4.6 Statistical analysis, error distribution and uncertainty estimation

We follow the same steps to calculate the error of each measured vector described by Charonko and Vlachos [32]. Our model is used to estimate the uncertainty of the magnitude of velocity error $\delta_{\vec{v}}$, which is calculated as:

$$\text{Error Magnitude (|Error M|)} = \sqrt{\delta_{\vec{v},i}^{\,2}} = \sqrt{\left(u_i - u_{i_{true}}\right)^2 + \left(v_i - v_{i_{true}}\right)^2} \tag{32}$$

where u_i and v_i are the measured velocities in horizontal and vertical direction of the i^{th} measurement respectively and $u_{i_{true}}$ and $v_{i_{true}}$ are the true values of velocities at the same point. After we calculate the values of the metrics mentioned before and the error of all the vectors in the two synthetic image data sets, we divided all the data points into 40 bins based on the value of the calculated metrics. Charonko and Vlachos have shown that the difference between the absolute magnitudes of mean velocity error and absolute mean error plus the standard deviation was very small[32], therefore they used $rms\delta_{\vec{v}}$ for the error distribution of each bin, calculated as:

$$rms\delta_{\vec{v}} = \sqrt{\left(mean(\delta_{\vec{v},i}{}^2)\right)} = \sqrt{\frac{1}{N}\sum_{i=1}^{N}\delta_{\vec{v},i}{}^2} \tag{33}$$

They also assumed that the error distribution of PIV measurement follows normal (Gaussian) distribution. Thus the coverage factor of $U_{68.5}$ uncertainty should reflect the probability that the true error stays within one standard deviation range. For normal distribution, the theoretical value for one standard deviation is 68.5%. However, this assumption was not tested at the time. Moreover in their analysis the $U_{68.5}$ uncertainty range was consistently over predicted with values of 81.4% for SCC and 76.1% for RPC, suggesting that the error distribution is likely not Gaussian.

In this work, we now test the validity of this hypothesis carefully analysing the error distribution type of PIV measurements. For example, Figure 7a shows the histogram of SCC error magnitude in the bin where PPR value is 1.5; 26727 data points were included in this bin. The solid gray line shows a Gaussian function based on the model Charonko and Vlachos used[32], where the mean value is fixed at 0 and the standard deviation value is the root-mean-square value of the error magnitude in of this bin. The dash line is the Gaussian function curve fitting based on the histogram and the solid black line represents the lognormal function curve fitting based on the histogram. More details can be seen when zoomed in, as shown in Figure 7b. It is obvious that the data do not

follow a Gaussian (normal) distribution and a lognormal distribution might provide a better approximation.

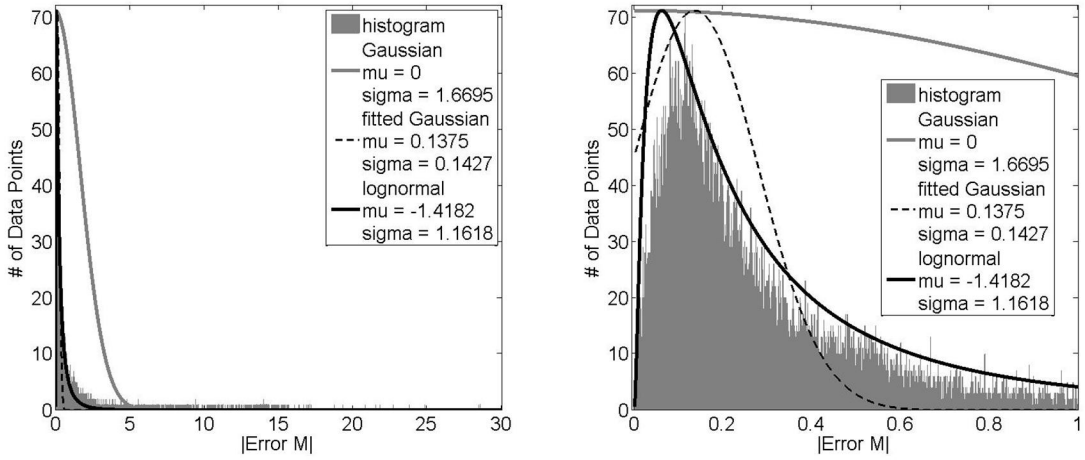

(a) (b)

Figure 7 Histogram and different distribution fitting of error magnitude at PPR = 1.5 (a) whole range of error; (b) zoomed in error < 1 region

We did the same test as shown above across all the range of available data. A few examples of histogram and the fitted curves error distribution function are shown in Figure 8. It is clear that across the whole range of PPR value, the lognormal fitting provides a better performance than Gaussian fitting especially at the tail regions. However, the lognormal fitting is still not a good match to the histogram at the tail region. As shown in all figures in Figure 8, the lognormal fitting curve is still lower than the outline of the histogram in the tail region. Other types of distributions were also checked and across all the range of available data. Although the lognormal fitting appeared to perform best, for several cases (not shown here) was not adequate or a Gaussian fit would perform better. These observations led to the realization that, without *a-priori* knowledge, it would not be appropriate to make any assumptions for the type of the error distribution. By checking the histogram of the PIV error magnitude, two important facts were discovered: first, the error distribution is not symmetric, suggesting that we should include two different parameters for

upper and lower limit of the uncertainty instead of using only one parameter as in previous work [32]; second, it is not appropriate to assume that the distribution of PIV error magnitude must follow a certain predefined function.

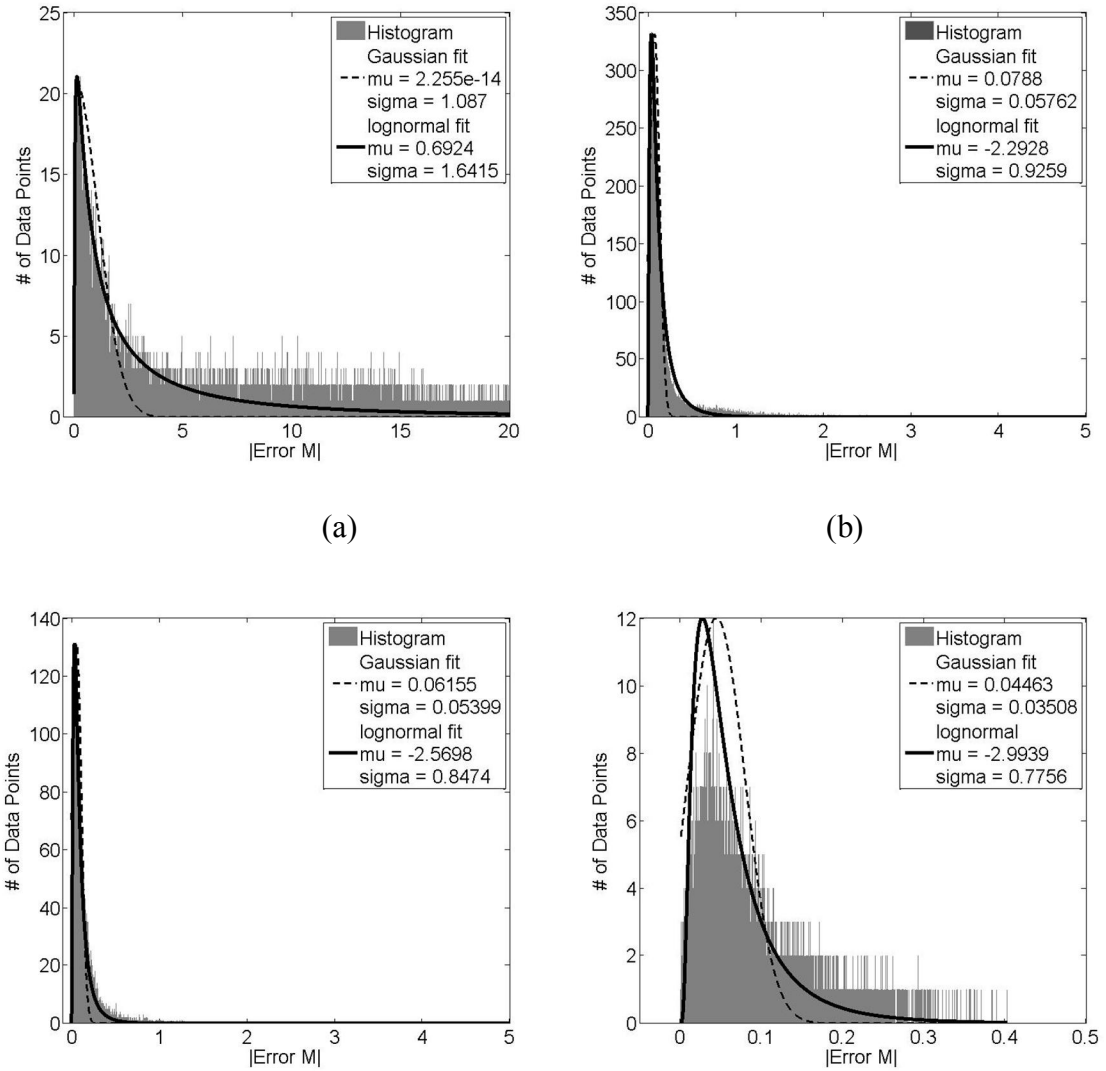

Figure 8 Histogram and different distribution fitting of error magnitude at (a) PPR = 1.0; (b) PPR = 3.0; (c) PPR = 5.9; (d) PPR = 9.9

Therefore, for developing models for PIV uncertainty estimation, instead of using the value of error magnitude, we calculate the upper and lower limit of the uncertainty based on the histogram of the binning as described in the previous paragraph. We keep using 68.5% and 95% confidence level

for $U_{68.5}$ and U_{95} uncertainty, which means 68.5% and 95% of all the data have the error magnitude smaller than the predicted uncertainty calculated by our model. Figure 9 is an example of calculating the upper and lower limit for U_{95} uncertainty of the bin with PPR value of 9.9. As shown in the figure, e_{low} is the lower limit indicating the point where the area under the curve is 2.5% of total area under the error magnitude histogram; e_{high} is the upper limit and 97.5% of the total area is under the curve on the error magnitude histogram. For $U_{68.5}$ uncertainty, the ratios are changed to 15.75% and 84.25% for lower and upper limit respectively. This approach allows robust estimation of the uncertainty coverage without any a-priori assumption of an error distribution function.

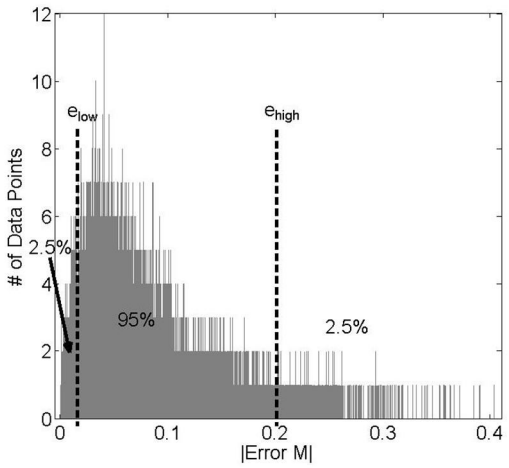

Figure 9 Example of calculating upper and lower limit for expanded uncertainty

5 Basic cross correlation signal-to-noise-ratio (SNR) model

5.1 Relationship of uncertainty versus cross-correlation SNR metrics

The uncertainty model which provides a relationship between any of the SNR metrics to the $U_{68.5}$ and U_{95} uncertainty limits are based on a fitting function proposed by Charonko and Vlachos[32]. The relationship between the SNR metrics and error are shown in Figure 10, Figure 11, and Figure 12 (markers); three different regions can be clearly observed. In each metric's low SNR value region, the error is dominated by the invalid measurements. A single-sided Gaussian with arbitrary width and magnitude and a center at the theoretical minimum value of the metric could fit the curve in this region. The dominant part of the error distribution is the error of valid measurements in the second region; the statistics of the displacement error (upper and lower limits for both the $U_{68.5}$ and U_{95} uncertainties) here decrease linearly with respect to the SNR metrics in a log-log scale plot. This suggests that a power law fitting should be appropriate. The trend appears to be levelling out at extremely large SNR metrics region for some cases, which corresponds to a constant part in the fitting function. This constant can be set to 0 for other cases, if the trend keeps going down as the SNR value increases. Combining all three different regions together, the upper and lower bounds of the estimated $U_{68.5}$ uncertainty and U_{95} uncertainty are calculated by determining the fitting parameters of the following equation:

$$U_x^2 = \left(M \exp\left(-\frac{1}{2}\left(\frac{\phi - N}{S} \right)^2 \right) \right)^2 + \left(A\phi^{-B} \right)^2 + C^2 \tag{34}$$

In above equations ϕ is the correlation SNR metrics, PPR, PRMSR, PCE and entropy; x indicates the confidence level, which is 68.5% or 95% in this work.

The first term is a Gaussian function used to account for the uncertainty due to invalid measurements which contribute uncertainty M, where the exact value of M is related to the range of possible velocity measurements and the distribution of the true velocity within the sampled flow

field [32]. The unit of M is in pixels. The $(\phi - N)$ term allows the error to climb rapidly as the metric's value approaches some small number, and N is the theoretical minimum value of the calculated metric.

Based on the definition of each quantity, we can determine analytically what value of N we should use for each metric. For PPR, the minimum value is Min(PPR) = 1 when we have a primary peak and secondary peak with the same height. Based on the definition of PRMSR, when all points in C_{rms} have a value of half the main peak height, the theoretical minimum value for PRMSR is Min(PRMSR) = 4. The extreme case for PCE occurs when the peak is only slightly higher than the rest of the correlation plane, and the rest of the plane shared the same correlation value; in this case the minimum PCE value Min(PCE) approaches 1. Because entropy behaves the opposite way as the other basic SNR metrics, we take the inverse of entropy, i.e. $\phi = 1/entropy$ to keep the fitting function type consistent among all metrics. Therefore, the theoretical minimum value for inverse entropy should be 0 as entropy approaches infinity.

The second term in equations 32, corresponding to a power-law, is used to calculate the contribution of the valid vectors to the uncertainty. If a given measurement is valid then A would govern the expected uncertainty. The last term C is a constant, which corresponds to the lowest uncertainty we can achieve. The units of A and C are in pixels. The estimated uncertainty for a measurement with a given calculated metric value is governed by the combination of the above three terms.

After the uncertainty on the magnitude of velocity error is calculated, we could split the uncertainty equally to the horizontal (U_u) and vertical (U_v) directions:

$$U^2 = U_u^2 + U_v^2 \tag{35}$$

However, in general the error is not isotropic, and this tends to overestimate the true uncertainty on one component and underestimated on the other.

Although invalid vectors are detected by using the new half peak diameter rule described earlier, it is not appropriate to develop a model for uncertainty estimation using only the valid measurements. Unlike synthetic image sets we used to build the model, in real experiments the true velocity field is unknown and it is inevitable that velocity fields would be contaminated by invalid measurements. Therefore both invalid and valid vectors are included in developing the uncertainty model estimation. However, if there is confidence that all measurements are valid, it could be appropriate to use only the second and third term from each fit. All synthetic cases with 3 different window size (or effective window size for RPC method), 16x16, 32x32, and 64x64 were included in the test providing a sample size containing about 3 million data points in total.

5.2 Result of uncertainty estimation

In order to keep the calculation process consistent, we applied the minimum correlation subtraction method as described earlier to both SCC and RPC. However, this method has a minimal effect on the RPC models. Figure 10 shows the curve fitting result for estimation the uncertainty using peak ratio with both RPC and SCC methods after the minimum subtraction.

The resulting curve fitting parameters for SCC and RPC are shown in Table 1. Where UL stands for upper limit and LL stands for lower limit. Where UL stands for upper limit and LL stands for lower limit. The values of the goodness of fit parameter, R^2, are also listed in Table 1.

Table 1 Fitting parameters of PPR.

	PPR							
	SCC				RPC			
	$U_{68.5UL}$	$U_{68.5LL}$	U_{95UL}	U_{95LL}	$U_{68.5UL}$	$U_{68.5LL}$	U_{95UL}	U_{95LL}
M	10.59	0.278	23.69	0.06816	25.11	0.09828	28.33	0.03258
N	1	1	1	1	1	1	1	1
S	0.1925	0.1927	0.2753	0.2446	0.2874	0.2258	0.7188	0.2406
A	0.6888	0.1043	4.112	0.03619	0.4583	0.09359	2.32	0.0359
B	0.846	0.6786	1.357	0.6342	0.5696	0.5597	0.8399	0.5681
C	0	0	0	0	0	0	0	0
R^2	0.98	0.97	0.98	0.97	0.97	0.95	0.98	0.94

In previously reported result for SCC processing, the fitting curve only partially agreed with the original data [32]. The current results shown in Figure 10a, show that the fit model provides agreement with the original data almost across the whole range, with R square value of 0.98 for the upper limit of $U_{68.5}$ uncertainty, 0.97 for the lower limit of $U_{68.5}$ uncertainty, 0.98 for the upper limit of U_{95} uncertainty and 0.97 for the lower limit of U_{95} uncertainty. The model for estimating uncertainty for SCC processing provides larger values by comparison to the RPC processing, which is anticipated since RPC has been shown to yield measurements with lower error. In the end, the current relationships yield an improved fit compared to those previously reported which did not use minimum subtraction of the correlation plane.

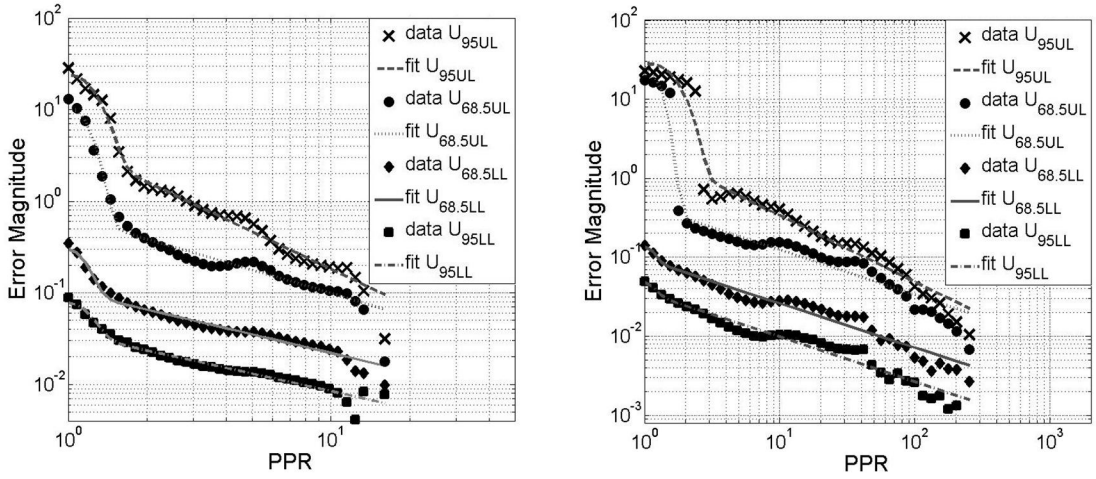

(a) (b)

Figure 10 Plots of the relationship of the calculated uncertainty on velocity versus peak ratio for both (a) SCC, and (b) RPC, for all synthetic image sets. (Markers) original curve of uncertainty bounds versus peak ratio; (Lines) three term function fitted curve.

The resulting fitting parameters of other metrics and the goodness of fit parameter, R^2, are listed in Table 2. Figure 11 shows the curve fitting results for estimating the uncertainty using

PRMSR and Figure 12 shows the results using entropy for both SCC and RPC methods. The fitting figures of PCE are similar to PRMSR, so they are not shown in this paper.

All the fit functions agree that the uncertainty would be larger for the SCC than the RPC for the same value of each metric. All these functions showed good agreement with the raw data, and the corresponding R square values are larger than 0.9.

Finally, the percent coverage of the $U_{68.5}$ and U_{95} uncertainty was calculated in comparison to the exact true error for each velocity vector measurement according to the following formula:

$$\text{coverage} = \frac{\#\text{ of estimateds for which } U_{68.5LL}(\text{or}\,U_{95LL}) \le \delta_{\bar{V}} \le U_{68.5UL}(\text{or}\,U_{95UL})}{\text{Total \# of velocity estimates}} \times 100\% \tag{36}$$

which calculates the percentage of measurements with true error values larger than the lower limits but smaller than the upper limits. The coverage should be close to 68.5% for the $U_{68.5}$ uncertainty and 95% for the U_{95} uncertainty if the uncertainty estimation was correct on average. The exact value of coverage factor of all functions using all synthetic data sets with 16x16, 32x32 and 64x64 window sizes are shown in Figure 13. In the work by Charonko and Vlachos [32], the authors showed that their method could only match the U_{95} uncertainty, it overestimated the $U_{68.5}$ uncertainty and the coverage factors were often greater than the theoretically expected value. It is important to note that because of the non-normal distribution of error for PIV measurements, this work shows that U_{95UL} cannot in general be approximated as $2U_{68.5UL}$, which helps explain the previous result. Their results also showed that the performance of SCC uncertainty prediction was inferior than that of RPC. For the present results, the coverage factors are much closer to the theoretical value for both $U_{68.5}$ uncertainty and U_{95} uncertainty with both SCC and RPC method. At $U_{68.5}$ uncertainty level, the SCC peak ratio (PPR) model provides the best match with a resulting coverage value of 68.27%; the worst cases is the SCC entropy model which has a coverage value of 66.58%. At U_{95} uncertainty level, the best match is the SCC peak ratio (PPR) model with resulting

coverage factor of 94.96%. Even for the worst case, the RPC entropy model, the difference between the result and the theoretical value is smaller than 1%.

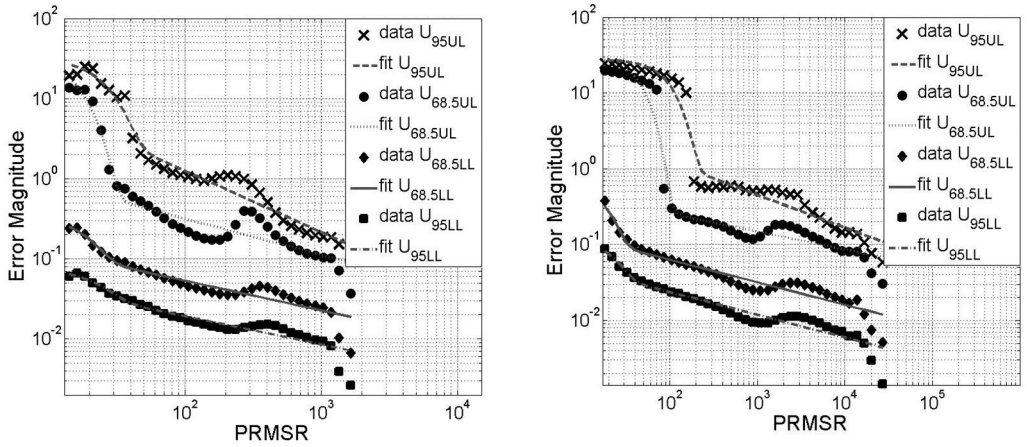

(a) (b)

Figure 11 Plots of the relationship of the calculated uncertainty on velocity versus PRMSR for both (a) SCC, and (b) RPC, for all synthetic image sets. (Markers) original curve of uncertainty bounds versus peak ratio; (Lines) three term function fitted curve

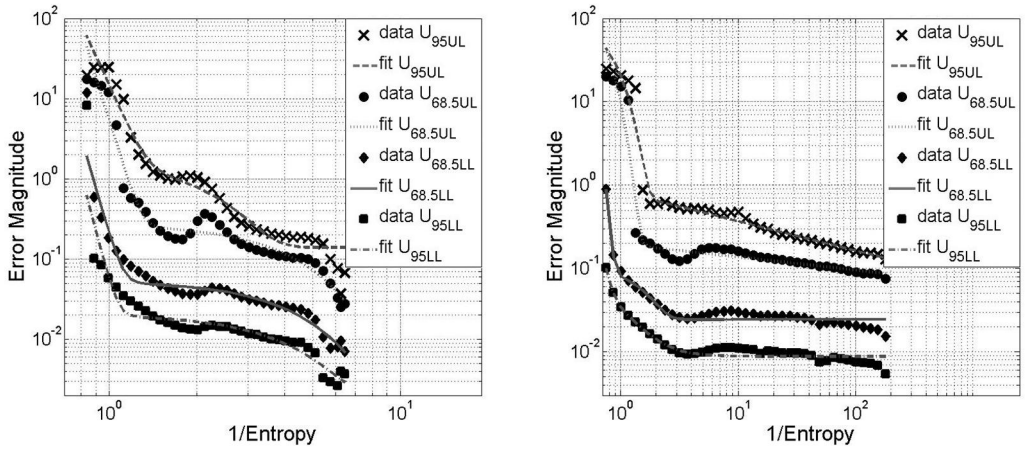

(a) (b)

Figure 12 Plots of the relationship of the calculated uncertainty on velocity magnitude versus Entropy for both (a) SCC, and (b) RPC, for all synthetic image sets. (Markers) original curve of uncertainty bounds versus peak ratio; (Lines) three term function fitted curve

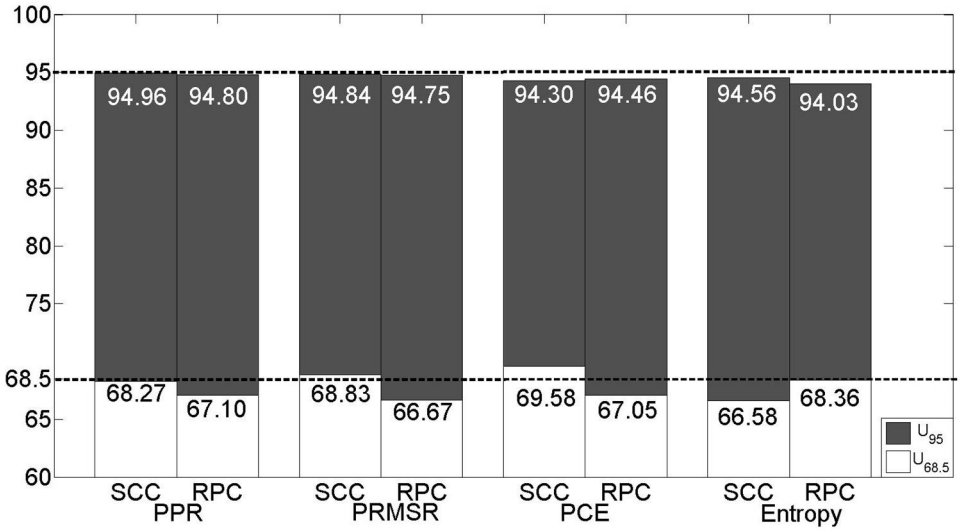

Figure 13 Coverage factors with synthetic image sets

Table 2 Fitting parameters of PRMSR, PCE and Entropy

	PRMSR							
	SCC				RPC			
	$U_{68.5UL}$	$U_{68.5LL}$	U_{95UL}	U_{95LL}	$U_{68.5UL}$	$U_{68.5LL}$	U_{95UL}	U_{95LL}
M	30.81	0.304	30.5	0.05974	29.93	0.5268	27.45	0.09569
N	4	4	4	4	4	4	4	4
S	9.806	13.04	17.8	18.45	32.49	13.23	76.7	17.92
A	2.494	0.2928	41.98	0.09639	0.7614	0.2461	8.852	0.09377
B	0.4498	0.3712	0.7634	0.3516	0.2369	0.297	0.4312	0.3006
C	0	0	0	0	0	0	0	0
R^2	0.95	0.91	0.97	0.91	0.97	0.93	0.97	0.92
	PCE							
	SCC				RPC			
	$U_{68.5UL}$	$U_{68.5LL}$	U_{95UL}	U_{95LL}	$U_{68.5UL}$	$U_{68.5LL}$	U_{95UL}	U_{95LL}
M	23.04	6.027	30.74	0.2045	30.28	37.77	29.38	0.1044
N	1	1	1	1	1	1	1	1
S	7.565	2.965	11.42	0.5224	23.79	3.837	47.76	14.29
A	1.639	1.108	29.08	0.5224	0.6188	0.7006	4.204	0.09491
B	0.3989	0.7855	0.7533	0.8713	0.2203	0.5618	0.3569	0.3268
C	0	0.0279	0	0	0	0.02047	0	0
R^2	0.95	0.94	0.97	0.92	0.76	0.92	0.94	0.90
	Entropy							
	SCC				RPC			
	$U_{68.5UL}$	$U_{68.5LL}$	U_{95UL}	U_{95LL}	$U_{68.5UL}$	$U_{68.5LL}$	U_{95UL}	U_{95LL}
M	0.2739	0.05352	1.757	0.02047	307	0.1039	118.3	2.181
N	0	0	0	0	0	0	0	0
S	3.076	3.188	3.056	3.063	0.3834	1.258	0.5364	0.2975
A	5.527	0.02148	14.7	0.05605	0.1982	0.01667	0.8363	0.03248
B	-11.59	-12.25	-7.985	-13.41	-0.1566	-13.92	-0.3523	-1.528
C	0	0	0.1407	0.001905	0	0.02452	0	0.008889
R^2	0.96	0.93	0.86	0.96	0.95	0.94	0.97	0.93

5.3 Application to experimentally measured flow fields

Our uncertainty models were further tested with real experiment data. In this work, we are using the same data set of stagnation plate flow used by Charonko and Vlachos [32]. The experiment set-up details can be found in [46]. The details of calculating the time average field and the uncertainty introduced by the fitting process were also described in [32].

After the correlation SNR and true error values for all measured vectors were calculated, we followed the same steps described in section 2.5 to bin the data and find the error distribution. The markers in Figure 14 show the relationship between PPR and the true error for RPC. The same trend described in section 7.1 has been observed in this figure: at the low PPR region, the error rapidly climbs up as the PPR value decreases, and the error decreases linearly with respect to the PPR value in a log-log scale at the region which the PPR values are relatively high. The lines in Figure 14 show the uncertainty estimated using the model listed in Table 1 combined (in a root-sum-square manner) with the uncertainty introduced by the fitting process. The values of the goodness of fit parameter, R^2, of the lower and upper limits for $U_{68.5}$ and U_{95} uncertainty between the experiment and the prediction are 0.77, 0.91, 0.85 and 0.88 respectively. Although these values are not as good as the ones reported for the synthetic results, they are still acceptable and the fits follow the error distribution with good agreement. Differences are larger for the higher PPR values where the model seems to underestimate the true uncertainty.

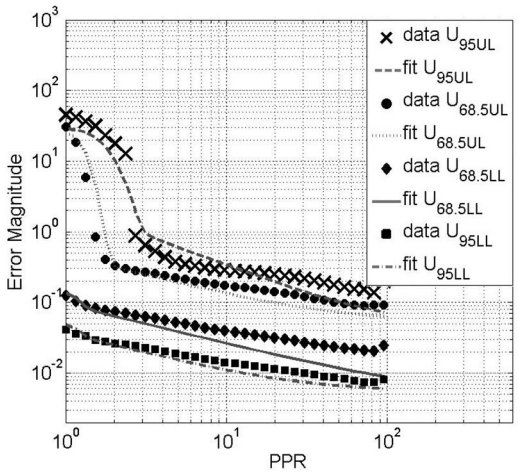

Figure 14 Plots of the relationship of the calculated uncertainty on velocity versus peak ratio for RPC, for real experiment. (markers) true error; (lines) estimated uncertainty based on Table 1.

The reported coverage factors are 73.5% for the $U_{68.5}$ uncertainty and 95% for the U_{95} uncertainty in Charonko and Vlachos' work [32]. The coverage results are improved in our work, especially for the $U_{68.5}$ uncertainty, by applying the corrections mentioned in the previous sections. The exact values of coverage factor of each metric using the real experimental dataset with 32x32 window sizes are shown in Figure 15. The SCC peak to root-mean-square ratio (PRMSR) model performs the best for both standard uncertainty and expanded uncertainty; the resulting coverage values are almost identical to the theoretical values, 68.51% for $U_{68.5}$ uncertainty and 95.03% for U_{95} uncertainty. At $U_{68.5}$ uncertainty level, the worst case is RPC peak ratio (PPR) model, which has the coverage factor of 63.26%. At U_{95} uncertainty level, the RPC peak to correlation energy (PCE) model performs the worst, it overestimated by 2.8%. The differences between the calculated values and theoretical coverages stay within less than 5% for all cases.

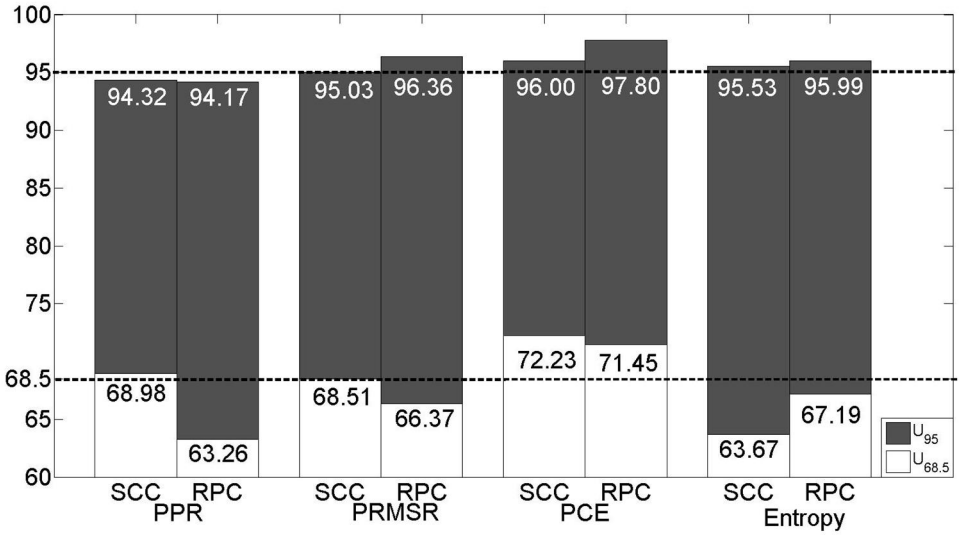

Figure 15 Coverage factors from the experimental data set.

Figure 16(a) shows the magnitude of the error (calculated using equation 10) on a representative instantaneous flow field, processed using SCC method. The peak ratio for each vector in this frame is shown in Figure 16(b), and the reverse pattern is seen. The upper limit of the $U_{68.5}$ uncertainty calculated from our SCC PPR model of each measured vector is plotted in Figure 16 (c), the pattern of the instantaneous uncertainty is quite similar to the error magnitude (Figure 16 (a)). However, the magnitude of predicted uncertainty is larger than the error magnitude. This is because in Figure 16 (c) what we plot is the upper limit of $U_{68.5}$ uncertainty, which means statistically about 84% of the error will be less than the value we predict. In fact, about 90% of error estimates are less than the uncertainty value we calculated from our model. The resulting coverage is shown in Figure 16 (d), the pixel will be set in color gray if the error magnitude of the measured vector at that location stays within the predicted upper and lower limit range; if the error magnitude is out of the predicted range, it will be colored in black. The total coverage factor for this frame is 62.46%. However, although this estimate only includes 64x80 (5120) data points, the difference

between the calculated coverage and the expectation stays within 10%, and when the analysis is expanded to the full data set the agreement is improved, as previously shown in Figure 15.

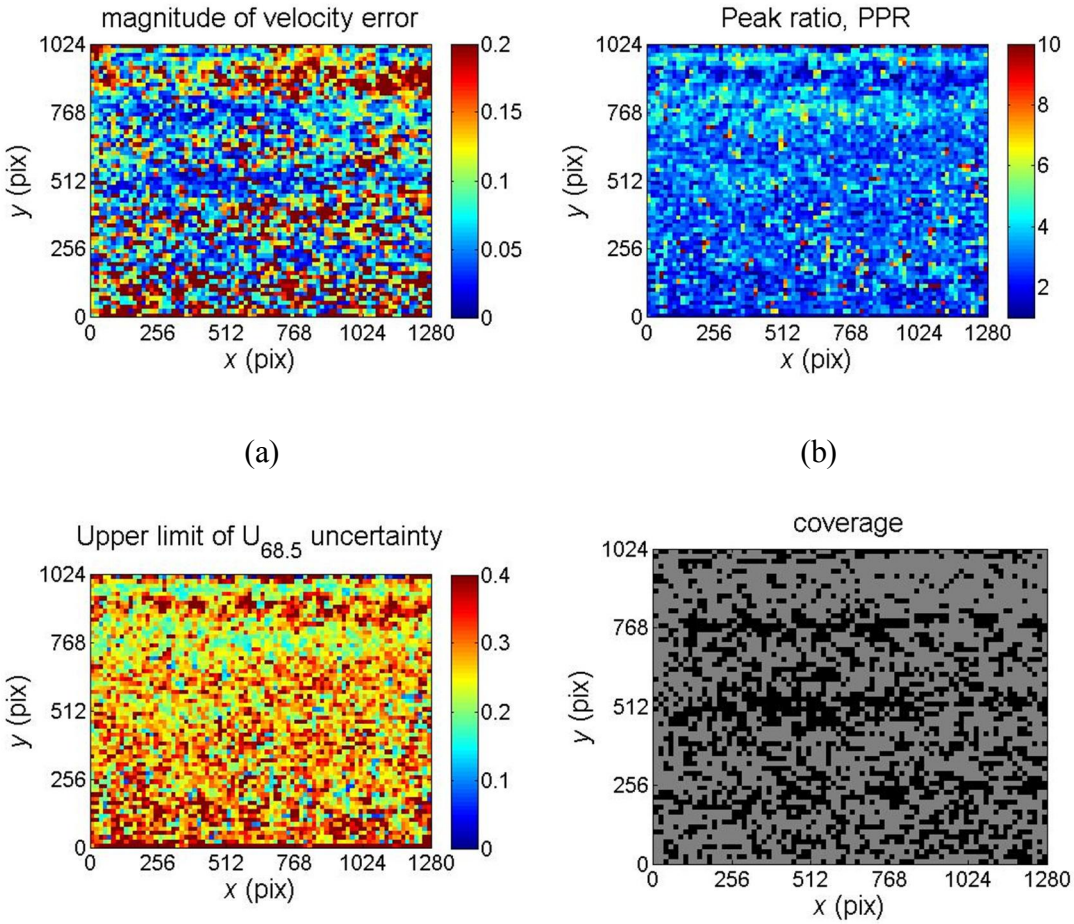

Figure 16 (a) Magnitude of estimated displacement error for a representative instantaneous flow field. (b) Peak ratios, PPR for the same frame. (c) Upper limit of $U_{68.5}$ uncertainty for the same frame calculated by SCC PPR model. (d) Coverage ($U_{68.5LL}$ < Magnitude of error < $U_{68.5UL}$), gray indicates the error of the measured vector stays within the estimated uncertainty range while black indicated a failure in estimating the uncertainty bounds.

6 Mutual information model

6.1 Mutual information (MI)

As shown in equation (28), the MI is a generalized form of the $N_I F_I F_O$, combining the effects of particle intensity distribution and diameter and these effects can be simplified as one scaling factor. To support this idea, PIV standard image sets were tested. An example comparison of MI and $N_I F_I F_O$ is presented in Figure 17 and Figure 18 using an image pair from the PIV standard image collection. Image region of interests (ROIs) are cropped to a window size of 32x32 pixels, a typical window size used in PIV processing. Particle locations and their identification number are provided with the images, dictating which particles are correlated between frames. Based on the provided particle list there are 60 particles in the first frame (left panel) and 57 particles in the second frame (right panel). Traditional $N_I F_I F_O$, when applied to the selected ROI frames, would return a value equal to the number of common particles shared by both frames. By referencing the particle list, it can be determined that these frames would return an $N_I F_I F_O$ value of 56. As mentioned in the theoretical derivation section, in standard PIV processing (using standard cross-correlation) the intensity and size of each particle contribute to the peak magnitude in the correlation plane. Therefore, particle diameter and intensity should be used to properly scale the $N_I F_I F_O$ value to obtain a better representation of the strength of correlation. We applied three point Gaussian fit on the particles to estimate the sizes of each particle. The scaled $N_I F_I F_O$ is calculated using equation (37), where I_{i1} and d_{i1} are the intensity and diameter of the i^{th} particle in frame 1 and I_{i2} and d_{i2} are the intensity and diameter of the i^{th} particle in frame 2. I_{max} is the maximum intensity, for this example, the value is 239.98, d_{mean} is the average particle diameter, in this case the value is 2.91. We also provide the intensity and diameter values of the three marked particles in Figure 17 as examples for calculation. The final result is 25.62 when we sum up the contribution of all 56 correlated particle pairs:

$$
\begin{aligned}
\left(\mathrm{N_I F_I F_O}\right)_{scaled} &= \sum_{i=1}^{N=56}\left(\frac{\sqrt{I_{i_1} I_{i_2}}}{\mathrm{I_{max}}} * \frac{\sqrt{d_{i_1} d_{i_2}}}{d_{\mathrm{mean}}}\right)^2 \\
&= \left(\left(\frac{\sqrt{I_{1_1} I_{1_2}}}{\mathrm{I_{max}}}\frac{\sqrt{d_{1_1} d_{1_2}}}{d_{\mathrm{mean}}}\right)^2 + \left(\frac{\sqrt{I_{2_1} I_{2_2}}}{\mathrm{I_{max}}}\frac{\sqrt{d_{2_1} d_{2_2}}}{d_{\mathrm{mean}}}\right)^2 + \left(\frac{\sqrt{I_{3_1} I_{3_2}}}{\mathrm{I_{max}}}\frac{\sqrt{d_{3_1} d_{3_2}}}{d_{\mathrm{mean}}}\right)^2 + \ldots\right) \\
&= \left(\left(\frac{\sqrt{72.65*72.28}}{239.98}\frac{\sqrt{3.16*2.83}}{2.86}\right)^2 + \left(\frac{\sqrt{219.60*218.60}}{239.98}\frac{\sqrt{3.56*2.78}}{2.86}\right)^2 \right. \\
&\quad \left. + \left(\frac{\sqrt{118.24*116.56}}{239.98}\frac{\sqrt{2.81*2.06}}{2.86}\right)^2 + \ldots\right) \\
&= 0.099 + 1.008 + 0.169 + \ldots \\
&= 25.62
\end{aligned}
\tag{37}
$$

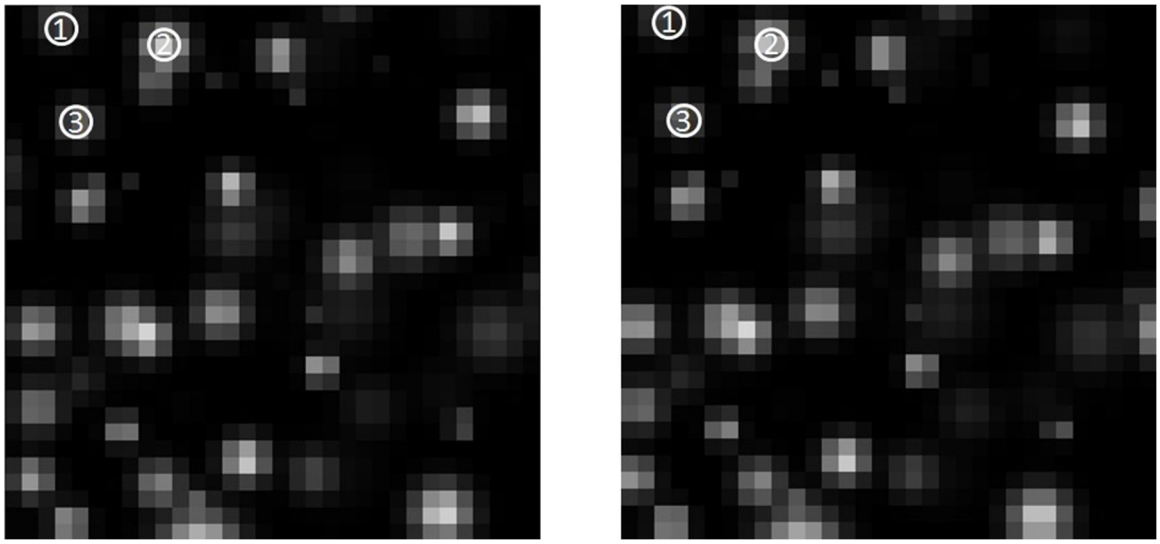

Figure 17: Example consecutive frames of particle images of PIV standard image case. The particles marked as the same number are the correlated particles based on the provided particle list.

The corresponding MI calculation using the same ROI images is shown in Figure 18. We followed the same step in section 2.1 to build the equivalent synthetic Gaussian particle. The average maximum intensity and the average mean particle diameter were calculated from these two interrogation regions. The left image from Figure 18 shows the standard cross-correlation plane calculated by applying standard cross correlation to the two ROI images shown in Figure 17. The right image of Figure 18 shows the autocorrelation of one representative synthetic particle pair. The

final result of MI is calculated using equation (38), resulting in a value closely matching the scaled $N_I F_I F_O$.

$$\mathrm{MI} = \frac{C_{\max}}{A_0} = \frac{1.113e6}{4.508e4} = 24.69 \tag{38}$$

The relationship between MI and intensity scaled $N_I F_I F_O$ is shown in Figure 19. It is clear that most of the results are aligned along the light gray dashed line corresponding to MI = $N_I F_I F_O$, supporting the notion that the MI provides a direct estimate of the apparent $N_I F_I F_O$ for an individual image pair. Some of the apparent scatter in the relationship is likely due to the inaccuracy of estimating the particle diameter by three point Gaussian fitting.

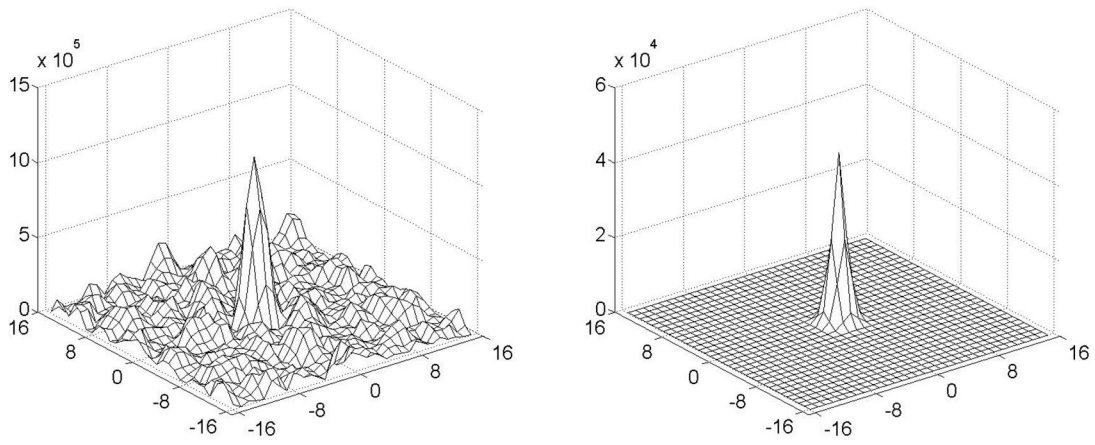

(a) (b)

Figure 18: (a) cross correlation plane calculated by SCC to the image sets in Figure 17; (b) the autocorrelation plane of one equivalent synthetic particle pair of image sets in Figure 17.

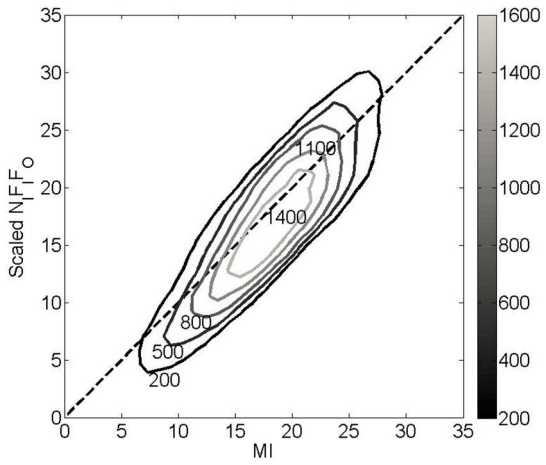

Figure 19: Mutual Information (MI) vs. $N_IF_IF_O$ Gray scaled contour plot represents number of measurements in each combination of calculated MI and exact $N_IF_IF_O$ value; The X-axis shows the value of MI and the Y-axis shows the value of intensity scaled $N_IF_IF_O$; light gray dash line shows where MI is equal to $N_IF_IF_O$ (MI = $N_IF_IF_O$).

To further demonstrate that MI can be used as a practical surrogate of the $N_IF_IF_O$ for an experiment, a linear function was fit to the data set with the intercept fixed at 0. The fitting function is shown in equation (39). The slope is 0.971, with an R^2 value for this fitting of 0.994, indicating that the fit agrees well with the raw data. Although this equation provides a way to convert MI back to $N_IF_IF_O$, it should not be used to get the "true" value of $N_IF_IF_O$. The $N_IF_IF_O$ value here is the intensity scaled value. When working with real experimental measurements, the $N_IF_IF_O$ values calculated using equation (39) would still be smaller than the traditional $N_IF_IF_O$ values.

$$N_IF_IF_O = 0.971\text{MI} \tag{39}$$

The relationship between the MI and the distribution of velocity error for Case B of 2003 PIV Challenge using standard cross correlation method with 32x32 window size is shown in Figure 20. The error $\delta_{\vec{v}}$ is defined as the magnitude of the velocity error. The root-mean-square value of the magnitude of velocity error, $rms\delta_{\vec{v},i}$ for the error distribution is calculated as:

$$rms\delta_{\vec{v},i} = \sqrt{\left(mean(\delta_{\vec{v},i}^{\ 2})\right)} = \sqrt{\frac{1}{N}\sum_{i=1}^{N}\delta_{\vec{v},i}^{\ 2}} = \sqrt{\frac{1}{N}\sum_{i=1}^{N}\left[\sqrt{\left(u_i - u_{i_{true}}\right)^2 + \left(v_i - v_{i_{true}}\right)^2}\right]^2} \quad (40)$$

where u_i and v_i are the measured velocities in the horizontal and vertical direction of the i^{th} measurement respectively and $u_{i_{true}}$ and $v_{i_{true}}$ are the true values of velocities at the same point. Details of statistical analysis and error distribution calculation are provided in [32]. The scatter plot shows all the combinations of MI and true error. It is obvious that large errors are present when the MI values are small. As shown in Figure 20, almost no measurements had both large error and high MI value in this case. Moreover, MI shows a 95% valid detection probability for MI values larger than 5 and when the MI value is below 5, the probability drops rapidly, both of which observations are consistent with previous findings for the valid vector detection probability versus $N_I F_I F_O$ [33].

In this section, we used synthetic PIV image sets to test the relationship between MI and $N_I F_I F_O$ (scaled). As mentioned in the previous section, the traditional definition of $N_I F_I F_O$ is inconsistent with the definition of the cross correlation, since it treats all particles contributing equally to the final correlation peak. Supported by the results presented in this section, we can claim that our MI method successfully overcomes this problem by directly using the information on the correlation plane. The MI metric makes it possible to directly estimate the effective number of correlated particle pairs in a less computational expensive way for the first time since the term $N_I F_I F_O$ appeared in the literature in 1990.

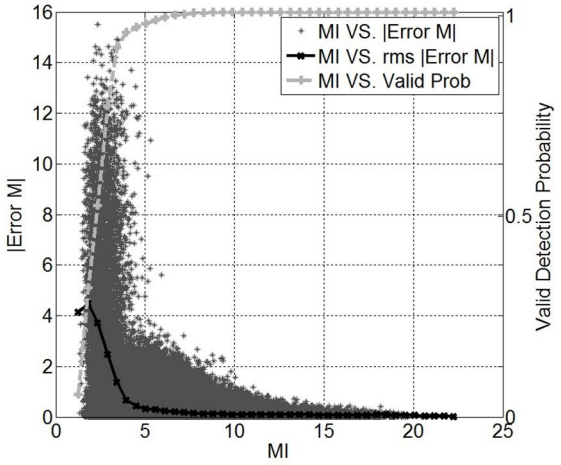

Figure 20: Plot of the distribution of velocity error using SCC processing versus correlation mutual information for the 2003 PIV Challenge case B. (scatter dot *) MI versus velocity error magnitude of each measured vector; (solid line) rms error of velocity magnitude (in units of pixel/frame) on each MI value; (dash line) valid detection probability on each MI value.

6.2 Relationship of uncertainty versus mutual information (MI)

6.2.1 Uncertainty analysis model

Our model is used to estimate the uncertainty of the magnitude of velocity error. The uncertainty models which provide a relationship between MI to the $U_{68.5}$ uncertainty and U_{95} uncertainty are based on a fitting function proposed in [47]. Hence, the estimated uncertainties are calculated by determining the fitting parameters of the following equations:

$$U_x^2 = \left(M \exp\left(-\frac{1}{2}\left(\frac{\mathrm{MI} - N}{S} \right)^2 \right) \right)^2 + \left(A\mathrm{MI}^{-B} \right)^2 + C^2 \tag{41}$$

where x indicates the confidence level, which is 68.5% or 95% in this work.

The first Gaussian term is used to account for the uncertainty due to invalid measurements. The maximum amount of uncertainty that comes from invalid measurements is governed by parameter M. N is the theoretical minimum value of MI, which is 0 for the limiting case when there is no

particle pair correlated between two consecutive image frames, and *S* controls the fall off of the probability for an invalid measurement. The second power law term is the contribution to the uncertainty by the valid vectors. The value of parameter *A* shows the maximum value of uncertainty that could be expected for a given MI value for a valid measurement. The last constant part indicates the lowest uncertainty we can achieve, which is governed by parameter *C*. Details of all the parameters in these equations can be found in [47].

Both invalid and valid vectors were included in developing the uncertainty estimation model. Case B of 2003 PIV Challenge and Case B of 2005 PIV Challenge with 32x32 window size (or effective window size for RPC method) were included in the test, providing a sample containing 1 million data points.

6.3 Result of uncertainty estimation

Figure 21 shows the curve fitting results for estimation the uncertainty using mutual information with both RPC and SCC methods after the minimum subtraction. The corresponding curve fitting parameters for SCC and RPC are shown in Table 3. In the table, the subscript *UL* stands for upper limit and *LL* stands for lower limit as defined for the standard and expanded uncertainties in Section 2.2.

Table 3: Fitting parameters of MI.

	SCC				**RPC**			
	$U_{68.5UL}$	$U_{68.5LL}$	U_{95UL}	U_{95LL}	$U_{68.5UL}$	$U_{68.5LL}$	U_{95UL}	U_{95LL}
M	65.69	0.3874	63.51	0.2686	0.3367	0.0012	11.75	0.0003
N	0	0	0	0	0	0	0	0
S	0.9197	1.048	1.397	0.6758	3.575	0.0067	1.294	0.0020
A	1.101	0.1525	11.14	0.0681	0.1289	0.0479	1.248	0.0163
B	1.073	0.7294	1.68	0.9268	0.4222	0.3252	0.8526	0.2698
C	0.0980	0.0164	0.1635	0.0094	0.0662	0	0	0
R^2	0.99	0.99	0.98	0.96	0.98	0.87	0.96	0.81

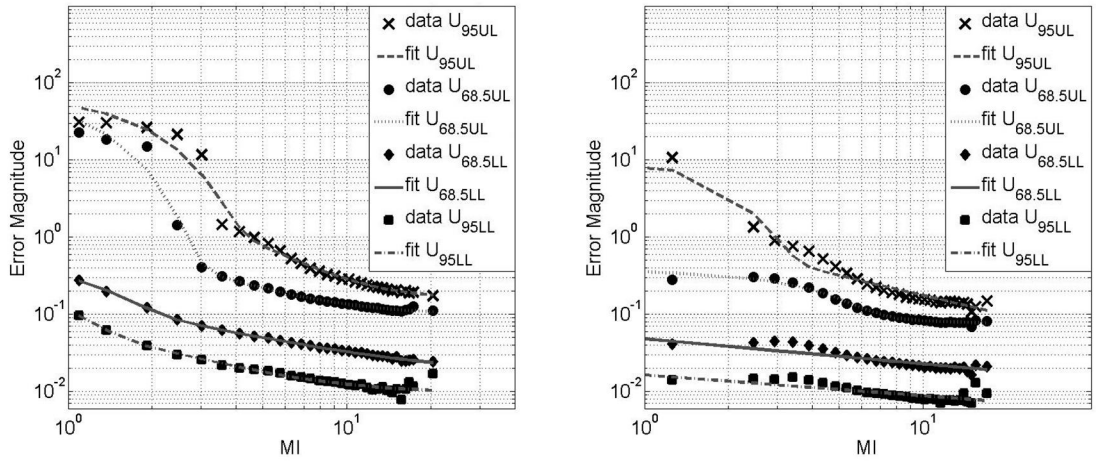

(a) (b)

Figure 21: Plots of the relationship of the calculated uncertainty on velocity magnitude versus correlation mutual information for both (a) SCC, and (b) RPC, for all synthetic image sets. (Markers) original curve of uncertainty bounds versus mutual information; (Lines) three term function fitted curve.

The values of the goodness of fit parameter, R^2, for all the fits are also listed in Table 3. In general, all the R^2 values are very close to 1, which means the agreement between fitting function and original data curve is acceptable.

It is interesting to note that the constant term in the SCC u_{UL} function is about 0.1 pixels, which indicates the average value of the lowest $\boldsymbol{U}_{68.5}$ uncertainty we can achieve is about 0.1 pixels. This fact matches well with the widely accepted value about the expected accuracy of PIV measurements under ideal (numerical simulation) conditions [28]. In general, RPC method will most likely give a better accuracy than SCC when dealing with the same particle image. Our uncertainty fitting models agree with this idea and the RPC function we have is similar to SCC with smaller values for all fitting parameters.

Finally, the percent coverage factors of the standard and expanded uncertainties were calculated in comparison to the exact true error for each velocity vector measurement according to the following formula:

$$\text{coverage} = \frac{\#\text{ of estimateds for which } U_{68.5LL}(\text{or}\,U_{95LL}) \le \delta_{\bar{V}} \le U_{68.5UL}(\text{or}\,U_{95UL})}{\text{Total \# of velocity estimates}} \times 100\% \tag{42}$$

which calculates the percentage of measurements with true error values larger than the lower limits but smaller than the upper limits. The coverage should be close to 68.5% for the $U_{68.5}$ uncertainty and 95% for the U_{95} uncertainty if the uncertainty estimation was correct on average. The exact values of coverage factors of all functions using the synthetic data sets are listed in Figure 22. All of the coverage factors are close to the theoretical values.

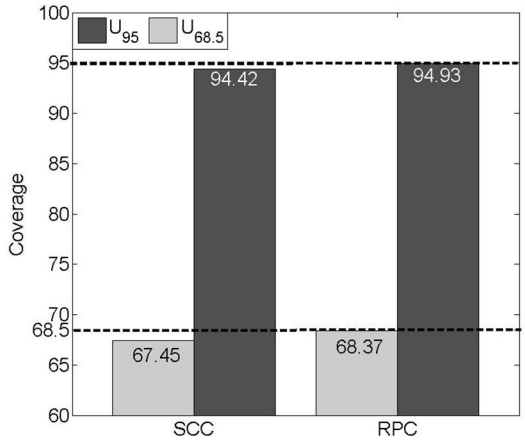

Figure 22: Coverage factors of all fitting functions with synthetic data sets.

Histograms for the magnitude of velocity error, upper and lower bounds of $U_{68.5}$ uncertainty, 15.75% and 84.25% percentile lines of the magnitude of velocity error for the entire data set are presented in Figure 24. If the uncertainty prediction model is working properly, the two percentile lines will stay close to the peaks in the histograms of estimated uncertainty bounds (in the case of a Gaussian distribution), as shown in the figures. The statistics of the error and estimated uncertainty bounds are listed in Table 5. For both models, the values of percentiles of true error are very close

to the mean and median values of the estimated uncertainty bounds. The shift between the peak and the percentile line (especially apparent for the upper limits) is due to the non-normal distribution of error and predicted uncertainty. These plots combine data from all points, but the error and uncertainty vary from point to point so the predicted uncertainty should not exactly match the bounds for the whole set. The true error distribution is skewed, so the uncertainty bounds should also reflect the same behavior. As shown in both Figure 23 and Table 4, both the UL and LL have skewed distributions similar to the true error.

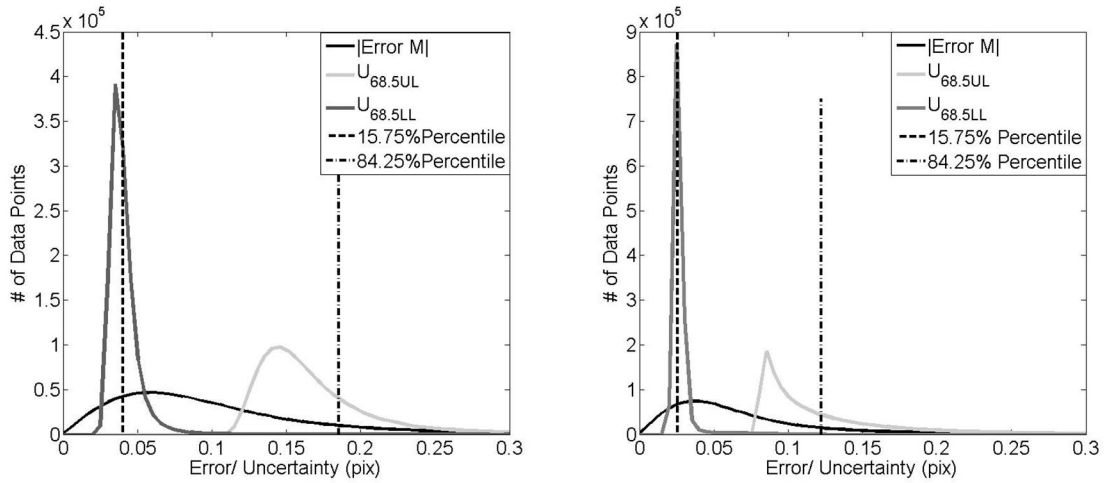

Figure 24: Plots for the histogram of true error (black), upper (light gray) and lower (dark gray) bound of estimated uncertainty and 15.75% (dash) and 84.25% (dash-dot) percentile of all data points of (a) SCC, and (b) RPC, for all synthetic image sets.

Table 5: Statistics of the error and uncertainty histogram.

	SCC	**RPC**
15.75% percentile	0.0402	0.0257
Mean $U_{68.5}$	0.0405	0.0271
Median $U_{68.5}$	0.0383	0.0258
84.25% percentile	0.1853	0.1221
Mean $U_{68.5}$	0.2155	0.1283
Median $U_{68.5}$	0.1585	0.1057

6.4 Application to real flow fields

Our uncertainty models were further tested with real experimental data. In this work, we are using the same data set of stagnation plate flow previously used by Charonko and Vlachos [32]. The experiment details can be found in [46]. The details of calculating the "exact solution" field and then the uncertainty introduced by the fitting process were described in [32].

The histograms of the MI values for both invalid and valid measurements of the entire data set are shown in Figure 25. There are about 400,000 data points in the invalid measurement subset and 15,000,000 data points in the valid measurement subset. About 60% of invalid measurements have MI values less than 2, with the peak of the histogram for the invalid measurements near the value of 1. The MI values for the valid measurements are larger, and only about 5% of valid measurements have the MI values less than 2. The peak of the histogram for the valid measurements is located at about 3. The results shown in Figure 25 agree with previous results that low MI values indicate that the number of correlated particle pairs is insufficient to construct a cross correlation plane with high correlation strength and the probability of an incorrect measurement will increase.

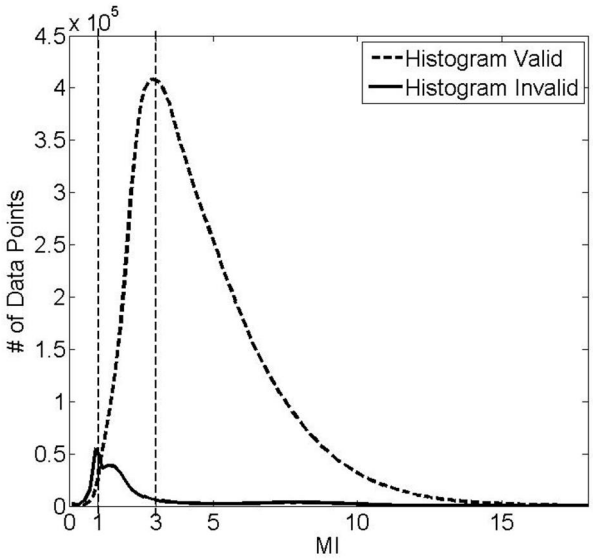

Figure 25: Histogram of the MI values for both invalid (solid line) and valid (dash line) measurements.

Figure 26 shows the rms values of the true error (calculate using equation (40)) of all valid measurements for the entire flow field. According to Charonko and Vlachos, a significant

contributor to the error is peak locking [32]. The same pattern is shown in this figure: the error levels are relatively low near the lines of integer displacement compared with those in the regions far away from the lines. The spatial distribution of the mean values of true errors and the estimated uncertainty bounds along a vertical slice is shown in Figure 27. Again, only valid measurements are included in the analysis. As shown in the figure, the peaks and valleys appear on the magnitude of velocity error curve correspond to the cyclic variation of error levels around the integer displacement values. The trends of the spatial distribution of uncertainty bounds follow the trend of the mean error spatial distribution (especially apparent for the upper limits), and the error stays within the provided ranges for most of the time. However, the cyclic bias errors are only partially reflected in the mean uncertainty bounds, suggesting that values determined from the MI level mostly measures the random error component of uncertainty.

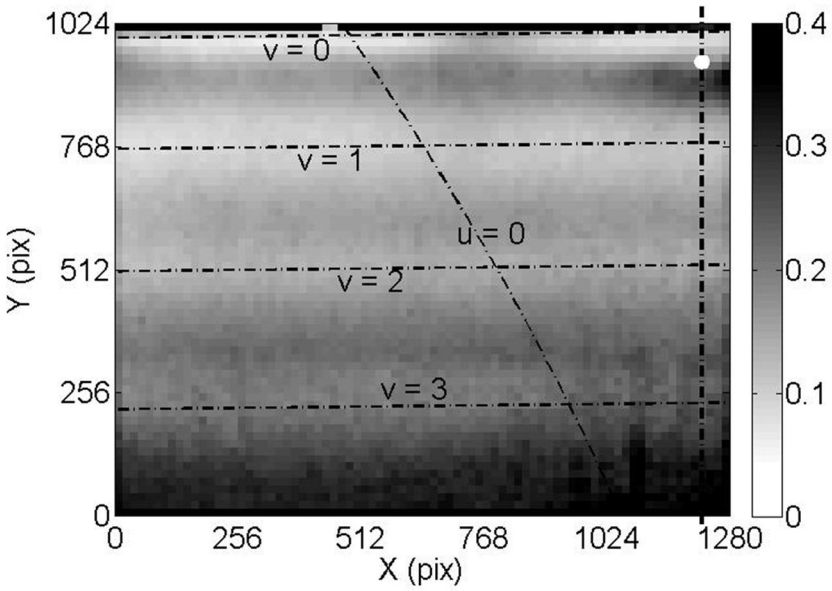

Figure 26: RMS value of magnitude of velocity error for the entire flow field (Gray scaled contour); contours of integer displacement for the mean flow field (white dash lines); the location of the vertical slice of the spatial distribution plot in Figure 27(black dash-dot line); the white dot near the top right corner is the location of the point of the time trace plot in Figure 28.

Figure 28 shows a time trace of the magnitude of true velocity error and the estimated uncertainty ranges of a point close to the right corner of the region near the stagnation plate (locate at (1224,952) in pixel coordinates, white dot in Figure 26) for the first 500 frames. For some frames, the MI values are very close to 0 thus making the values of the upper limit for both standard and expanded uncertainties extremely high (even larger than 10). However, those points are not shown in Figure 28. The true error stays within the range provided by the estimated uncertainty bounds for most of the time, as shown in the figure. The coverage factors of this set of samples, which includes 500 data points, for the $U_{68.5}$ uncertainty and U_{95} uncertainty are 66.8% and 99% respectively.

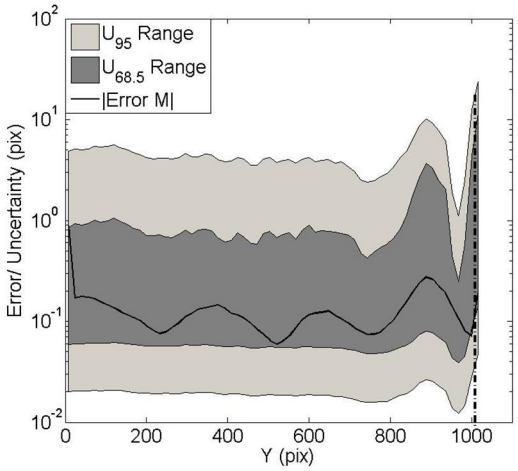

Figure 27: Spatial distribution of mean magnitude of velocity error value (black), mean estimated $U_{68.5}$ uncertainty range (dark gray) and mean estimated U_{95} uncertainty range (light gray) long a vertical line located near the right edge of the image (black dash-dot line in Figure 26); the location of the stagnation plate (black dash-dot line).

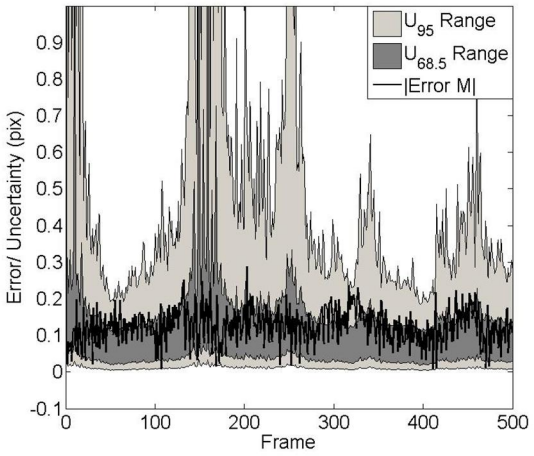

Figure 28: Time trace plot of the true value of magnitude of velocity error (black), estimated $U_{68.5}$ uncertainty range (dark gray) and estimated U_{95} uncertainty range (light gray) of one velocity vector located close to the stagnation plate (at (1224,952) in pixel coordinates, white dot in Figure 26)

The resultant total coverage is shown in Figure 29. The exact values of coverage factor of each metric using the entire real experiment data set with 32x32 window sizes are also listed. Values of all coverage factors are close to the target values.

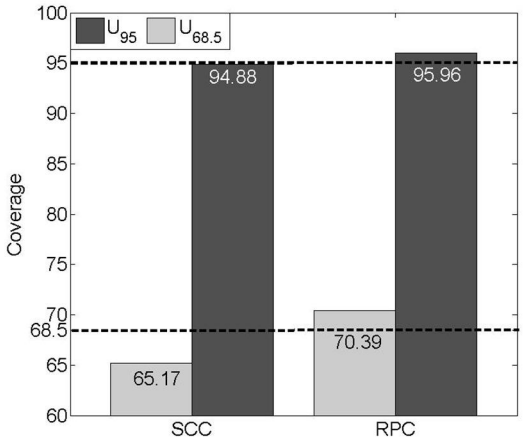

Figure 29: Coverage factors for fitting functions with real experimental data

Finally, Charonko and Vlachos showed that the correlation strength based PIV uncertainty estimation model generalizes to multi-pass methods [32]. We applied the same idea here to test the

MI model. A series of 1000 frames of the real experimental data was processed using a 2 pass discrete window offset SCC method. The grid resolution and the interrogation window size were set to a 16x16 pixel grid resolution and 32x32 pixel window size. The error histogram, $U_{68.5}$ uncertainty upper and lower bounds histogram and the 15.75% and 84.25% true uncertainty percentiles for both passes are shown in Figure 30. Statistics are listed in Table 6. As shown in the figure, comparing pass 2 with pass 1, more data points appear in the small error/ uncertainty region. The percentile lines for both upper and lower limits of true $U_{68.5}$ uncertainty shift to the left, which also means by applying multi-pass method, the uncertainty of the PIV measurement will decrease. As described in the previous section, the two percentile lines remain near the peaks of estimated uncertainty bounds, and the mean and median values of the estimated uncertainty bounds are close to the values of the percentiles of the true error for both passes.

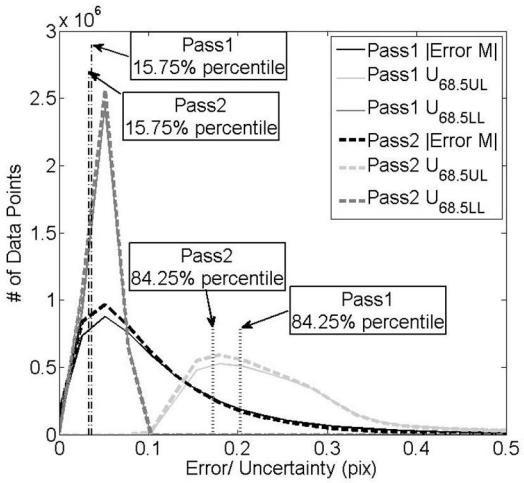

Figure 30: Plots for the histogram of true error and the estimated uncertainties for pass 1 and 2 of an iterative discrete window offset processing using the SCC method on the experimental data. Line styles are similar to Figure 24, with estimated pass 1 uncertainty denoted by solid lines, and by dashed lines for pass 2.

Table 6: Statistics of the error and uncertainty histogram.

	Pass1	**Pass2**
15.75% percentile	0.0364	0.0334
Mean $U_{68.5}$	0.0494	0.0488
Median $U_{68.5}$	0.0493	0.0481
84.25% percentile	0.2026	0.1726
Mean $U_{68.5}$	0.2736	0.2643
Median $U_{68.5}$	0.2310	0.2243

7 Conclusion

In this thesis, we show that cross-correlation SNR metrics calculated exclusively from the correlation plane can be used to estimate the uncertainty of the PIV measurement. In the first part of our work, the metrics of basic correlation SNR related to the peak detectability are introduced. We also develop a new metric termed Mutual information (MI) to estimate the real and apparent $N_I F_I F_O$ directly from the calculated correlation plane. Both theoretical derivation and experiment results support that MI corresponds to the apparent $N_I F_I F_O$ and would be a practical measure of the correlation SNR with direct connection to the established PIV theory. A simple but consequential correction on the correlation plane is introduced using a minimum correlation value subtraction to remove the effect of the background image noise and thus improve the model's performance for uncertainty estimation. Moreover we redefine the concept of invalid measurement using the correlation peak diameter in order to formulate a definition that is consistent with the uncertainty estimation framework. Finally, in the process of developing uncertainty prediction models we also show that the PIV measurement error distribution cannot be simply assumed to follow a certain known distribution function, and new models with upper and lower uncertainty limits calculated from the error histogram are established, thus first correcting for overestimation errors introduced by a Gaussian distribution assumption but also enabling the development of explicit expressions for the upper and lower limit of $U_{68.5}$ and U_{95} uncertainties in our models with the specified confidence intervals.

The relationships between the uncertainty and the metrics of correlation SNR of individual velocity measurements were explored using both robust phase correlation (RPC) and standard cross correlation (SCC) method. The uncertainty is governed by a well-defined relationship between the correlation SNR using a three-term formulation for both processing methods. In the three-term function, the Gaussian distribution term is related to probability of occurrence of invalid

measurements; the power-law term describes the primary behavior of the uncertainty versus the metrics; and a constant expressing the minimum expected uncertainty level for the corresponding methodology, regardless of value of the metrics. The formulas successfully predict the $U_{68.5}$ and U_{95} uncertainty coverage close to 68.5% and 95% over the synthetic image sets as well as a 2D stagnation point experiment case using all provided metrics and both the SCC and RPC method.

In conclusion, this work generalizes a framework for models predicting the expected uncertainty levels for individual velocity measurements in a PIV flow field without the knowledge of image quality and local flow conditions using only the information contained in the calculated correlation plane. This work continues efforts establishing the foundations toward the growing understanding of PIV uncertainty estimation.

Nomenclature

A, B, C	fitting coefficients for the uncertainty vs. correlation SNR in eqs. (32) and (40)
$A(s,t)$	autocorrelation of particle image pairs
A_0	magnitude of autocorrelation
a	local velocity gradient
C	tracer number density
C_{max}	primary peak height
C_2	height of the secondary peak
C_{rms}	root mean square value of the cross correlation plane
C(i)	correlation value of the i^{th} point on the correlation plane
D_I	linear dimension of interrogation area
d_D	primary peak diameter
d_τ	particle image diameter
d_i	diameter of the i^{th} particle
E_c	correlation energy
$F_O(\Delta z)$	out-of-plane loss of correlation
$F_\tau(s,t)$	particle self-correlation
$F_I(s,t)$	in-plane loss of correlation
$I(X,Y)$	light intensity distribution
$\langle I_{1,2} \rangle$	mean particle image intensity
$\Delta I_{1,2}$	fluctuation particle image intensity
$\boldsymbol{J}_0$	maximum value of illuminating beam intensity
J_i	intensity of the i^{th} particle

M_0	nominal image magnification
MI	mutual information between two frames
M, N, S	fitting coefficients for uncertainty vs. correlation SNR in eqs. (32) and (40)
N_I	image density
$P(X,Y)$	image of one representative particle
p	number of particles appear in the interrogation window
PPR	primary peak ratio
PRMSR	peak to root mean square ratio
PCE	peak to correlation energy ratio
R	spatial cross correlation of two particle image patterns, which can be further divided into components originating from the correlation of background and fluctuating components of the image (R_C, R_F, R_D) as described in the text [2]
R_C	cross correlation of the uniform background components of each particle image pattern
R_F	cross correlation of the uniform background of one image with the fluctuating part of the other image
R_D	cross correlation of the fluctuating part of each particle image pattern
RPC	Robust Phase Correlation, see refs [13, 14, 36]
s,t	displacement in horizontal and vertical direction
SCC	Standard Fourier-based Cross Correlation
W	size of the correlation plane
u_i , v_i	measured velocity in the horizontal and vertical direction of the i^{th} vector
$u_{i_{true}}$, $v_{i_{true}}$	true velocity in the horizontal and vertical direction of the ith vector
$\delta_{\bar{v}}$	magnitude of velocity error

$U_{68.5}$	expanded uncertainty for a 68.5% confidence interval, matching the one standard deviation level for a normal distribution
U_{95}	expanded uncertainty for a 95% confidence interval, matching the two standard deviation level for a normal distribution
$\Delta z_{12}^{''}$	thickness of the light sheet
ϕ	correlation SNR metrics
τ_{00}	total particle image intensity per unit illumination
$\tau(X,Y)$	particle image pattern
Ω	group of points on the correlation plane with correlation value lower than half of the primary peak

References

[1] Willert C E and Gharib M 1991 Digital particle image velocimetry Experiments in Fluids 10 181-93

[2] Adrian R J and Westerweel J 2011 Particle Image Velocimetry: Cambridge University Press)

[3] Meynart R 1983 Mesure de champs de vitesse d' ecoulements fluides par analyse de suites d' images obtenues par diffusion d' un feuillet lumineux. In: Facult'e des Sciences Appliqu'ees: Universite Libre de Bruxelles)

[4] Adrian R J 1984 Scattering particle characteristics and their effect on pulsed laser measurements of fluid flow: speckle velocimetry vs particle image velocimetry Applied Optics 23 1690-1

[5] Keane R D and Adrian R J 1990 Optimization of particle image velocimeters. I. Double pulsed systems Measurement Science and Technology 1 1202

[6] Keane R D and Adrian R J 1991 Optimization of particle image velocimeters: II. Multiple pulsed systems Measurement Science and Technology 2 963

[7] Adrian R J 2005 Twenty years of particle image velocimetry Experiments in Fluids 39 159-69

[8] Westerweel J 1997 Fundamentals of digital particle image velocimetry Measurement Science and Technology 8 1379

[9] Huang H T, Fiedler H E and Wang J J 1993 Limitation and improvement of PIV Exp Fluids 15 168-74

[10] Scarano F and Riethmuller M L 2000 Advances in iterative multigrid PIV image processing Experiments in Fluids 29 S051-S60

[11] Meinhart C D, Wereley S T and Santiago J G 2000 A PIV Algorithm for Estimating Time-Averaged Velocity Fields Journal of Fluids Engineering 122 285-9

[12] Westerweel J, Geelhoed P F and Lindken R 2004 Single-pixel resolution ensemble correlation for micro-PIV applications Exp Fluids 37 375-84

[13] Eckstein A, Charonko J and Vlachos P 2008 Phase correlation processing for DPIV measurements Experiments in Fluids 45 485-500

[14] Eckstein A and Vlachos P P 2009 Digital particle image velocimetry (DPIV) robust phase correlation Measurement Science and Technology 20 055401

[15] Soloff S M, Adrian R J and Liu Z-C 1997 Distortion compensation for generalized stereoscopic particle image velocimetry Measurement Science and Technology 8 1441

[16] Willert C 1997 Stereoscopic digital particle image velocimetry for application in wind tunnel flows Measurement Science and Technology 8 1465

[17] Scarano F 2002 Iterative image deformation methods in PIV Measurement Science and Technology 13 R1

[18] Scarano F 2003 Theory of non-isotropic spatial resolution in PIV Experiments in Fluids 35 268-77

[19] Scarano F 2004 A super-resolution particle image velocimetry interrogation approach by means of velocity second derivatives correlation Measurement Science and Technology 15 475

[20] Wereley S and Gui L 2003 A correlation-based central difference image correction (CDIC) method and application in a four-roll mill flow PIV measurement Experiments in Fluids 34 42-51

[21] Wereley S T and Meinhart C D 2001 Second-order accurate particle image velocimetry Experiments in Fluids 31 258-68

[22] Adrian R J 1991 Particle-Imaging Techniques for Experimental Fluid Mechanics Annual Review of Fluid Mechanics 23 261-304

[23] Grant I 1997 Particle image velocimetry: A review Proceedings of the Institution of Mechanical Engineers. Part C, Journal of mechanical engineering science 211 55-76

[24] Raffel M, Willert C E and Kompenhans J 1998 Particle image velocimetry : a practical guide (Berlin; New York: Springer)

[25] Kompenhans J, Kompenhans J and Westerweel J 2000 Particle image velocimetry: progress towards industrial application: Kluwer Academic Publishers)

[26] Westerweel J 2000 Theoretical analysis of the measurement precision in particle image velocimetry Exp Fluids 29 S003-S12

[27] Westerweel J 2008 On velocity gradients in PIV interrogation Exp Fluids 44 831-42

[28] Huang H, Dabiri D and Gharib M 1997 On errors of digital particle image velocimetry Measurement Science and Technology 8 1427

[29] Marcus M, Volker S and David L R 2002 Measurement of digital particle image velocimetry precision using electro-optically created particle-image displacements Measurement Science and Technology 13 997

[30] Timmins B, Wilson B, Smith B and Vlachos P 2012 A method for automatic estimation of instantaneous local uncertainty in particle image velocimetry measurements Experiments in Fluids 53 1133-47

[31] Sciacchitano A, Wieneke B and Scarano F 2013 PIV uncertainty quantification by image matching Measurement Science and Technology 24 045302

[32] Charonko J J and Vlachos P P 2013 Estimation of uncertainty bounds for individual particle image velocimetry measurements from cross-correlation peak ratio Measurement Science and Technology 24 065301

[33] Keane R and Adrian R 1992 Theory of cross-correlation analysis of PIV images Applied Scientific Research 49 191-215

[34] Hain R and Kähler C J 2007 Fundamentals of multiframe particle image velocimetry (PIV) Experiments in Fluids 42 575-87

[35] Persoons T and O'Donovan T S 2011 High Dynamic Velocity Range Particle Image Velocimetry Using Multiple Pulse Separation Imaging Sensors 11 1-18

[36] Eckstein A and Vlachos P P 2009 Assessment of advanced windowing techniques for digital particle image velocimetry (DPIV) Measurement Science and Technology 20 075402

[37] Kumar B V K V and Hassebrook L 1990 Performance measures for correlation filters Appl. Opt. 29 2997-3006

[38] Shannon C E 2001 A mathematical theory of communication SIGMOBILE Mob. Comput. Commun. Rev. 5 3-55

[39] Warner S O and Smith B L 2014 Autocorrelation-based estimate of particle image density for diffraction limited particle images Measurement Science and Technology 25 065201

[40] Brady M R, Raben S G and Vlachos P P 2009 Methods for Digital Particle Image Sizing (DPIS): Comparisons and improvements Flow Measurement and Instrumentation 20 207-19

[41] Brady M R, Raben S G and Vlachos P P 2009 Methods for Digital Particle Image Sizing (DPIS): Comparisons and improvements Flow Measurement and Instrumentation 1-13

[42] Westerweel J and Scarano F 2005 Universal outlier detection for PIV data Experiments in Fluids 39 1096-100

[43] Okamoto K, Nishio S, Kobayashi T, Saga T and Takehara K 2000 Evaluation of the 3D-PIV standard images (PIV-STD project) Journal of Visualization 3 115-23

[44] Stanislas M, Okamoto K, Kähler C J and Westerweel J 2005 Main results of the Second International PIV Challenge Experiments in Fluids 39 170-91

[45] Stanislas M, Okamoto K, Kähler C J, Westerweel J and Scarano F 2008 Main results of the third international PIV Challenge Experiments in Fluids 45 27-71

[46] Hubble D O, Vlachos P P and Diller T E 2013 The role of large-scale vortical structures in transient convective heat transfer augmentation Journal of Fluid Mechanics 718 89-115

[47] Xue Z, Charonko J J and Vlachos P P 2014 Particle image velocimetry correlation signal-to-noise ratio metrics and measurement uncertainty quantification Submit to Measurement Science and Technology arXiv:1405.3023